




# Methane storage in flexible and dynamical metal–organic frameworks


Cite as: Chem. Phys. Rev. **3**, 021308 (2022); <https://doi.org/10.1063/5.0072805>

Submitted: 24 September 2021 • Accepted: 15 March 2022 • Published Online: 27 May 2022

Katherine A. Forrest, Gaurav Verma, Yingxiang Ye, et al.

## COLLECTIONS

 This paper was selected as Featured

 This paper was selected as Scilight



View Online



Export Citation



CrossMark

## ARTICLES YOU MAY BE INTERESTED IN

[Flexible porous materials improve methane storage](#)

Scilight **2022**, 211110 (2022); <https://doi.org/10.1063/10.0011496>

[An International Standard Formulation for trans-1-Chloro-3,3,3-trifluoroprop-1-ene \[R1233zd\(E\)\] Covering Temperatures from the Triple-Point Temperature to 450#K and Pressures up to 100 MPa](#)

Journal of Physical and Chemical Reference Data **51**, 023101 (2022); <https://doi.org/10.1063/5.0083026>

[Optical measurements on a budget: A 3D-printed ellipsometer](#)

American Journal of Physics **90**, 445 (2022); <https://doi.org/10.1119/10.0009665>



Applied Physics  
Reviews

Read. Cite. Publish. Repeat.

**19.162**  
2020 IMPACT FACTOR\*

# Methane storage in flexible and dynamical metal–organic frameworks

Cite as: Chem. Phys. Rev. **3**, 021308 (2022); doi: [10.1063/5.0072805](https://doi.org/10.1063/5.0072805)

Submitted: 24 September 2021 · Accepted: 15 March 2022 ·

Published Online: 27 May 2022






View Online



Export Citation



CrossMark

Katherine A. Forrest,<sup>1</sup> Gaurav Verma,<sup>2</sup> Yingxiang Ye,<sup>2</sup> Junyu Ren,<sup>2</sup> Shengqian Ma,<sup>2</sup>  Tony Pham,<sup>1,a)</sup>   
and Brian Space<sup>3,a)</sup> 

## AFFILIATIONS

<sup>1</sup>Department of Chemistry, University of South Florida, 4202 East Fowler Avenue, CHE205, Tampa, Florida, 33620–5250, USA

<sup>2</sup>Department of Chemistry, University of North Texas, 1508 W Mulberry St, Denton, Texas 76201, USA

<sup>3</sup>Department of Chemistry, NC State University, 2620 Yarbrough Dr, Raleigh, North Carolina 27695, USA

<sup>a)</sup>Authors to whom correspondence should be addressed: [tpham4@mail.usf.edu](mailto:tpham4@mail.usf.edu) and [brian.b.space@gmail.com](mailto:brian.b.space@gmail.com)

## ABSTRACT

Recently, there has been significant interest in methane as an abundant and cleaner burning alternative to fossil fuels. Consequently, the design of media capable of the storage of methane under practical conditions has become an area of significant interest to the scientific community. While metal–organic frameworks have seen pronounced examination for this application, flexible metal–organic framework variants have been little examined despite having tremendous promise for methane storage applications. This work provides an overview of the current state of the art regarding the investigation of these systems for the purpose of providing a baseline for future research.

Published under an exclusive license by AIP Publishing. <https://doi.org/10.1063/5.0072805>

## TABLE OF CONTENTS

I. INTRODUCTION .....	1
II. BREATHING FRAMEWORKS.....	3
A. BDP series .....	3
B. Square pillared materials .....	5
C. MIL-53 series.....	5
D. X-dia-1-Ni .....	9
E. DUT-49.....	10
III. FLEXIBLE CONSTITUENTS.....	11
A. Conformational adjustment.....	12
B. Gate opening effects .....	12
C. Photo-catalyzed shifting.....	14
IV. COMPUTATIONAL STUDIES.....	15
V. DISCUSSION.....	16
VI. CONCLUSION.....	17

## I. INTRODUCTION

With a continuous increase in the global energy demand on one hand and catastrophic environmental degradation by overuse of fossil fuels on the other, it has become the need of the hour to transition to clean, efficient, and low-carbon footprint technologies. Although there has been an increasing use of renewables, it is expected that the renewable energy sources (solar, wind, geothermal, hydropower, biomass,

and nuclear fission) will be able to supply only 7% of total global energy demand by 2040.<sup>1</sup>

The use of natural gas in power plants and automobile industry, however, has gained escalating interest, and by 2040,<sup>2</sup> the demand for natural gas is expected to increase by 36%. Natural gas is a promising transition fuel for clean and renewable energy because of its abundance in nature, and it is relatively environmentally friendly. Methane (CH<sub>4</sub>) is the primary component of natural gas and has relatively 40% lower carbon dioxide (CO<sub>2</sub>) emissions compared to conventional fossil fuels.<sup>3,4</sup>

However, there are some technical constraints preventing the widespread use of natural gas such as the lack of refueling infrastructure and a low volumetric energy density of methane (0.04 MJ l<sup>-1</sup>) compared to liquid fossil fuels (32.4 MJ l<sup>-1</sup>) at ambient conditions. The Advanced Research Projects Agency-Energy (ARPA-E) of the US Department of Energy (DOE) has introduced several targets for methane on-board storage systems. The gravimetric target is to store 0.5 g(CH<sub>4</sub>) g<sup>-1</sup> (adsorbent) or 700 cm<sup>3</sup> (CH<sub>4</sub>) g<sup>-1</sup> (adsorbent), and the volumetric storage target is 263 cm<sup>3</sup> (standard temperature and pressure, STP) cm<sup>3</sup> cm<sup>-3</sup> at 298 K and 65 bar, which is equivalent to the energy density of compressed natural gas (CNG) at 250 bar. The volumetric storage target is set at a higher value of 350 cm<sup>3</sup> cm<sup>-3</sup> considering a 25% packing loss due to packing and palletization.<sup>3,5</sup>

These storage targets seem practical and have been achieved, but the efficiency of the adsorbent material depends on their deliverable

capacity (between 5 and 35/65 bar). The deliverable capacity (also known as working capacity and usable capacity) is defined as the usable amount of methane that can be obtained from the adsorbent upon reducing the adsorption pressure to the minimum inlet pressure (5 bar). It is calculated by subtracting the uptake at 5 bar from the uptake obtained at the maximum adsorption pressure (35/65 bar), as shown in Fig. 1.<sup>6</sup>

The last two decades have witnessed enormous advances in the field of porous metal–organic frameworks (MOFs),<sup>7</sup> and they have become promising candidates for natural gas storage and separation<sup>3,4,8</sup> because of their crystallinity, high porosity, structural tunability, ease of functionalization, and high density of active sites.<sup>9</sup> MOFs are built from metal ions/clusters and polytopic organic linkers forming infinite coordination networks.<sup>10</sup> The porous nature of these structures permits adsorption of incoming gas molecules onto their interior surface, binding the gas molecules and making them attractive for a number of gas sorption applications, including gas storage media.<sup>11</sup> Practical application for fuel storage requires strong enough binding that the gas can be stored with sufficient compaction, while weak enough that the captured molecules can be released for application.

MOF synthesis began in the 1990s<sup>12</sup> and the ease of synthesis leads to the creation of thousands of structures, but understanding of design principles lagged behind and structure design tailored to specific applications is still a field in development.

One of the earliest examples of MOFs used for high-pressure methane storage was  $\{[M_2(4,4'\text{-bpy})_3(\text{NO}_3)_4] \cdot x\text{H}_2\text{O}\}$  ( $M = \text{Co}, \text{Ni}, \text{and Zn}; 4,4'\text{-bpy} = 4,4'\text{-bipyridine}$ ) reported by the Kitagawa group in 1997 displaying moderate methane uptake capacity.<sup>13</sup> Yaghi *et al.* explored an isoreticular series of MOFs (IRMOF) having varied functionalities and linker length.<sup>14</sup> The IRMOF-6 displayed a high capacity for methane storage at  $240 \text{ cm}^3 \text{ (STP) g}^{-1}$  at 36 atm and ambient temperature. HKUST-1<sup>15</sup> built from copper(II) paddlewheel units and trimesic acid (1,3,5-benzenetricarboxylic acid) still holds the record highest volumetric uptake capacity of  $267 \text{ cm}^3 \text{ cm}^{-3}$  at 65 bar and room temperature among reported MOFs. However, owing to the Type I shape of the methane uptake isotherm it shows high value for the uptake at 5 bar, lowering the overall deliverable capacity to  $190 \text{ cm}^3 \text{ cm}^{-3}$ . Since then, a number of rigid MOFs with high volumetric uptakes under these conditions have been reported such as PCN-14<sup>16</sup> ( $230 \text{ cm}^3 \text{ cm}^{-3}$ ), MAF-38<sup>17</sup> ( $263 \text{ cm}^3 \text{ cm}^{-3}$ ), Ni-MOF-74<sup>15b</sup> ( $251 \text{ cm}^3 \text{ cm}^{-3}$ ), and MOF-519<sup>18</sup> ( $260 \text{ cm}^3 \text{ cm}^{-3}$ ); however, only a few of these MOFs exhibit high volumetric deliverable capacity such as MOF-519 ( $209 \text{ cm}^3 \text{ cm}^{-3}$ ), NJU-

Bai-43<sup>19</sup> ( $198 \text{ cm}^3 \text{ cm}^{-3}$ ), UTSA-76a<sup>20</sup> ( $197 \text{ cm}^3 \text{ cm}^{-3}$ ), MFM-115<sup>21</sup> ( $191 \text{ cm}^3 \text{ cm}^{-3}$ ), and HKUST-1 ( $190 \text{ cm}^3 \text{ cm}^{-3}$ ).<sup>15</sup>

Recently, many flexible MOFs exhibiting a S-shaped isotherm [Fig. 1(b)]<sup>6</sup> (also called a type IV or type F-IV isotherm) have been explored and they offer multiple advantages for gas storage and separation over rigid frameworks while retaining the desirable characteristics.<sup>22</sup> The multi-step adsorption isotherms enlarge the uptake difference between the charge and discharge pressures, making them attractive for practical gas storage and delivery.<sup>23</sup> These isotherms are preferable because the usable capacity depends on the gate-opening pressure. Additionally, the thermodynamic cost of fast heat exchange between the container and the environment is compensated by the structural phase transformation, which can consume/provide the heat generated/required during the adsorption/desorption cycles, respectively.<sup>6,24</sup> Thus, the flexible frameworks are of utmost interest in this regard as they can deliver a high methane payload.<sup>25</sup> For example, Co(bdp) (bdp = 1,4-benzenedipyrazolate) displays a deliverable capacity of  $197 \text{ cm}^3 \text{ cm}^{-3}$  at  $25^\circ\text{C}$  upon phase transition from a low porosity or non-porous to a porous phase.<sup>6</sup> Furthermore, it has been demonstrated that the steps of the isotherms can be tuned by varying the functionality, solvent, metal ion, and the guest molecule pressure.<sup>26</sup>

In this review, we have summarized the utilization of flexible MOFs for methane storage applications. To put the results of the review into a more general context, flexible MOFs appear to be a promising platform for storage of methane. The dual advantages of material expansion and subsequent enthalpic compensations as a result provide features difficult to achieve for rigid materials. This review demonstrates that chemical components necessary to create flexible materials are extant and further research is warranted; specifically, the bdp series described in Sec. II A demonstrates promise. This is the first in-depth review focusing specifically on methane storage in flexible and dynamical MOFs to the best of our knowledge. The methane storage in rigid adsorbents and stimulation of flexibility with other adsorbates such as  $\text{CO}_2$ , solvent molecules, and other guests, as well as more fundamental aspects of flexibility, have been extensively covered elsewhere<sup>27,51</sup> and are beyond the scope of this review. Notably, a literature survey of the important studies focusing on  $\text{CH}_4$  adsorption in various flexible MOFs is presented for the first time herein. The status of methane storage in different series of breathing frameworks and MOFs with local mobility is discussed and the factors influencing the gate opening/closing and the step isotherms are explored briefly. The representative MOFs discussed here are depicted in Fig. 2, and the

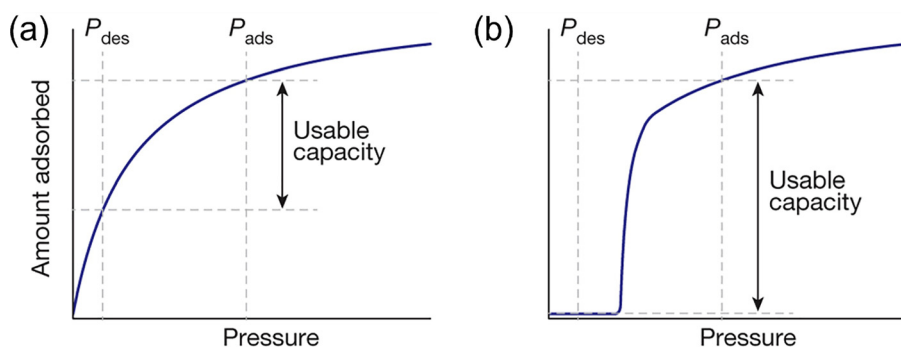


FIG. 1. Illustration of the deliverable capacity in (a) rigid adsorbents and (b) flexible adsorbents. Reproduced with permission from Mason *et al.*, *Nature* **527**, 357–361 (2015) Copyright 2015 Springer Nature.

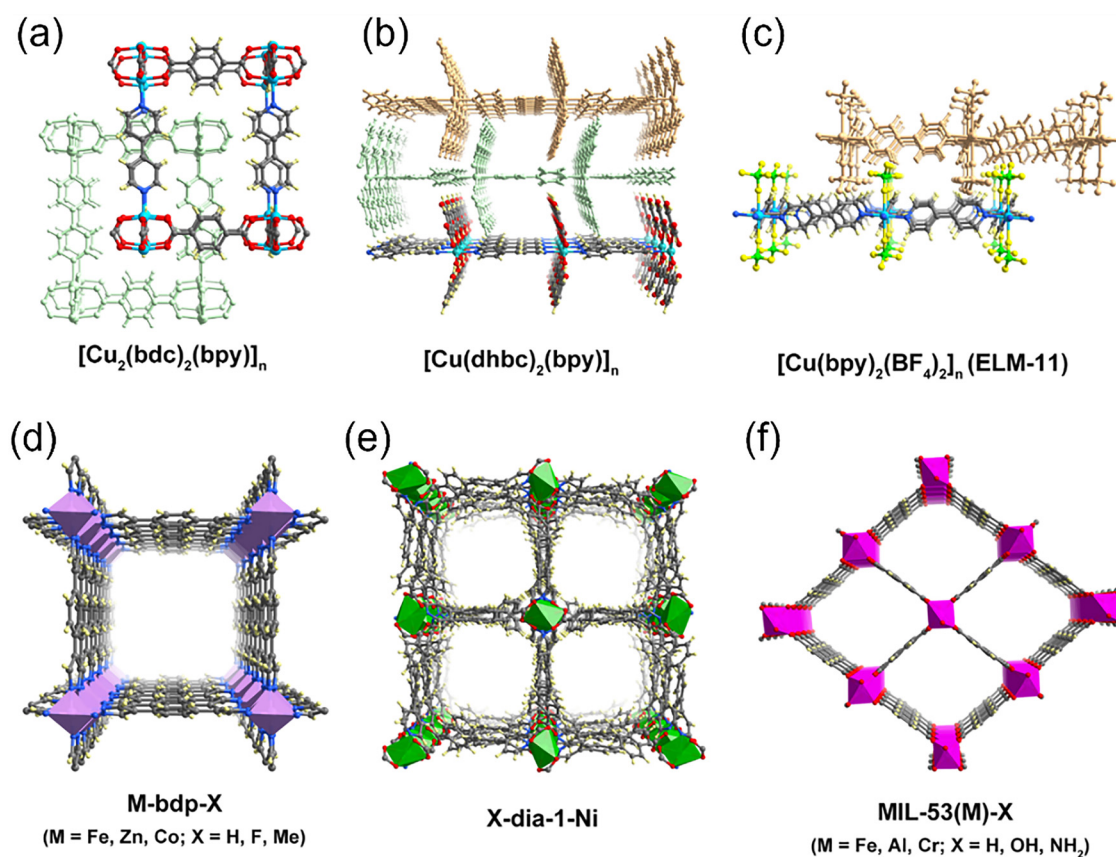


FIG. 2. Crystal structures of some representative flexible MOFs mentioned in this review.

manuscript is organized as follows: Sec. II discusses extant research into fully flexible MOF platforms and individual frameworks. Section III examines those structures with mobile elements contained in otherwise rigid scaffolds. A brief overview of the computational studies and methods is provided in Sec. IV. In Sec. V, a summary of the research progress so far and the structure–property relationships has been provided. Section VI discusses conclusions and outlook for future studies. While this paper aims to provide an overview of a large amount of research, we apologize to any authors whose work has been omitted in this review article due to oversight.

## II. BREATHING FRAMEWORKS

Breathing is a reversible phenomenon in which the relative distances, angles, and the orientation of the functional groups can change with external stimuli such as guest molecules, solvent, or temperature. The framework can go through several crystal phases triggered by the environmental conditions leading to a change in the cell volume whereby the amplitude of the transformation can be sometimes very significant. The corresponding change in the framework's cell volume can lead to narrow pore (np) or large pore (lp) phases and cause the gating effect that may prevent or facilitate the adsorption of a gas. This change also drastically affects the porosity leading to a significant

change in pore volume facilitating the adsorption of the guest due to opening of the pore channels/windows.

Various techniques such as *in situ* x-ray diffraction, gas adsorption, and nuclear magnetic resonance spectroscopy have been utilized to monitor the breathing behaviors of the MOFs upon exposure to heat, pressure, and gases. Theoretical calculations have also been employed for the elucidation of the principles of breathing behaviors using density and molecular dynamic simulations. It has been observed that the breathing behaviors of MOFs arise from the synergistic effects of strong guest–host and guest–guest interactions as well as the coordination symmetry of metal nodes and rotatable axis of the linkers.

Despite the variety of MOFs, only several classes exhibit the unique breathing phenomena. In this section, we focus on summarizing these classes of MOFs that show the breathing effect and their methane adsorption properties.

### A. BDP series

The M(bdp) series of MOFs (M = Co, Fe) reported by the long group display the highest deliverable capacities for methane among the flexible MOFs owing to their large internal surface areas and a high degree of flexibility.<sup>6</sup>

The solvated framework is comprised of square channels built from one-dimensional chains of tetrahedral  $M^{2+}$  cations that are bridged by the  $\mu_2$ -pyrazolates from the bdp [Fig. 3(a)]. For Co(bdp), the evacuated framework displays minimal uptake of methane at low pressures, and after reaching 16 bar, a sharp step in the adsorption isotherm is observed [Fig. 3(b)]. The desorption shows hysteresis and the loop is closed by 7 bar, indicating a reversible structural phase transformation from a non-porous to porous framework that could be fully reproduced over 100 adsorption–desorption cycles. The *in situ* powder x-ray diffraction (PXRD) studies under variable methane pressures further established the phase transition by the observance of a single collapsed phase under vacuum, followed by the appearance of new peaks corresponding to expanded phase from 17 to 23 bar and eventually conversion back to the fully collapsed phase between 10 and 5 bar during desorption. The Co(bdp) has a deliverable methane capacity of  $155 \text{ cm}^3 \text{ cm}^{-3}$  at 35 bar and  $197 \text{ cm}^3 \text{ cm}^{-3}$  at 65 bar at  $25^\circ\text{C}$ . These high values for the usable capacity result from the minimal uptake of less than  $0.2 \text{ mmol g}^{-1}$  at pressures below 5.8 bar.

In the case of Fe(bdp), the adsorption and the desorption steps occur at higher pressures of 24 and 10 bar, respectively [Fig. 3(c)], due to stronger interactions that lead to an increase in energy for the phase transition. The deliverable capacity for Fe(bdp) is still high at  $150 \text{ cm}^3 \text{ cm}^{-3}$  for 35 bar and  $190 \text{ cm}^3 \text{ cm}^{-3}$  for 65 bar adsorption at  $25^\circ\text{C}$ . The Fe(bdp) undergoes another expansion to a framework having nearly perfect square channels at pressures above 40 bar.

Both Fe(bdp) and Co(bdp) can also offer intrinsic heat management in the adsorption/desorption cycles by utilizing the enthalpy change during phase transition to offset the heats of sorption. The expansion is endothermic, and thus, the amount of heat released per

liter of adsorbent during transition from 5.8 to 35 bar is  $73.4 \text{ kJ}$  for Co(bdp) and  $64.3 \text{ kJ}$  for Fe(bdp), which is a reduction of 33% for the former and 41% of the latter compared to HKUST-1 ( $109 \text{ kJ l}^{-1}$ ). Thus, these frameworks provide a much-improved internal thermal management.

The stability of the collapsed phase of Co(bdp) is provided by the edge-to-face  $\pi \cdots \pi$  interactions present in the neighboring bdp ligands between the aryl rings. On the one hand, it provides the necessary driving force for the phase transition back to the collapsed phase; however, on the other hand, it leads to an increase in the gate opening pressure. Thus, the positives of thermal management and usable capacity are offset by costly initial compression that would be required at the storage and transport facilities. An ideal adsorbent is required to have the spread of the isotherm step in the DOE operational range of 5–35/65 bar.

Long *et al.*, thus, proposed the use of different functionalities on the central bdp ring in the Co(bdp) to alter the strength of the edge-to-face interactions and decrease/increase the step pressures. A series of derivatives Co(F-bdp), Co(p-F<sub>2</sub>-bdp), Co(o-F<sub>2</sub>-bdp), Co(p-Me<sub>2</sub>-bdp), and Co(D<sub>4</sub>-bdp) (F-bdp = 2-fluoro-1,4-benzenedipyrazolate; p-F<sub>2</sub>-bdp = 2,5-difluoro-1,4-benzenedipyrazolate; o-F<sub>2</sub>-bdp = 2,3-difluoro-1,4-benzenedipyrazolate; p-Me<sub>2</sub>-bdp = 2,5-dimethyl-1,4-benzenedipyrazolate; D<sub>4</sub>-bdp = 1,4-benzenedipyrazolate-d<sub>4</sub>) with different functional groups were obtained [Fig. 4(a)].<sup>28</sup>

The methane uptake isotherm of Co(D<sub>4</sub>-bdp) is nearly identical to that of the Co(bdp) with step pressure of  $\sim 18$  bar [Fig. 4(b)]. Co(p-Me<sub>2</sub>-bdp) displays no phase change below 70 bar due to increased strength and stabilization of the favorable edge-to-face  $\pi \cdots \pi$  interactions by the methyl groups in the collapsed structure.

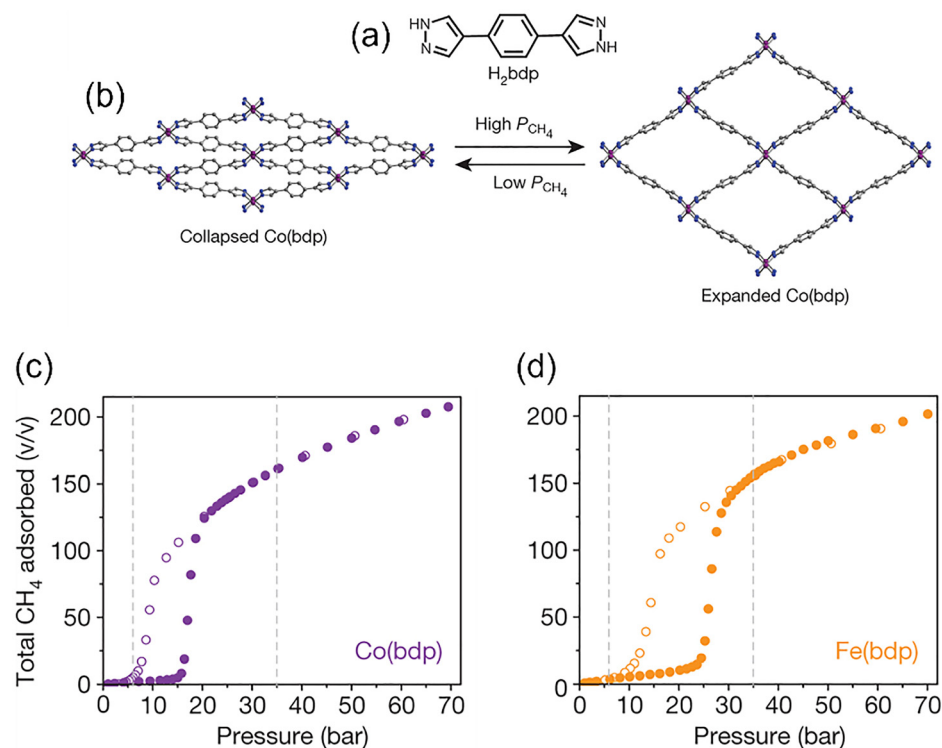


**FIG. 3.** (a) The ligand H<sub>2</sub>bdp and (b) structures of the expanded and the collapsed frameworks of Co(bdp). High-pressure methane adsorption isotherms of (c) Co(bdp) and (d) Fe(bdp). Reproduced with permission from Mason *et al.*, Nature **527**, 357–361 (2015) Copyright 2015 Springer Nature.

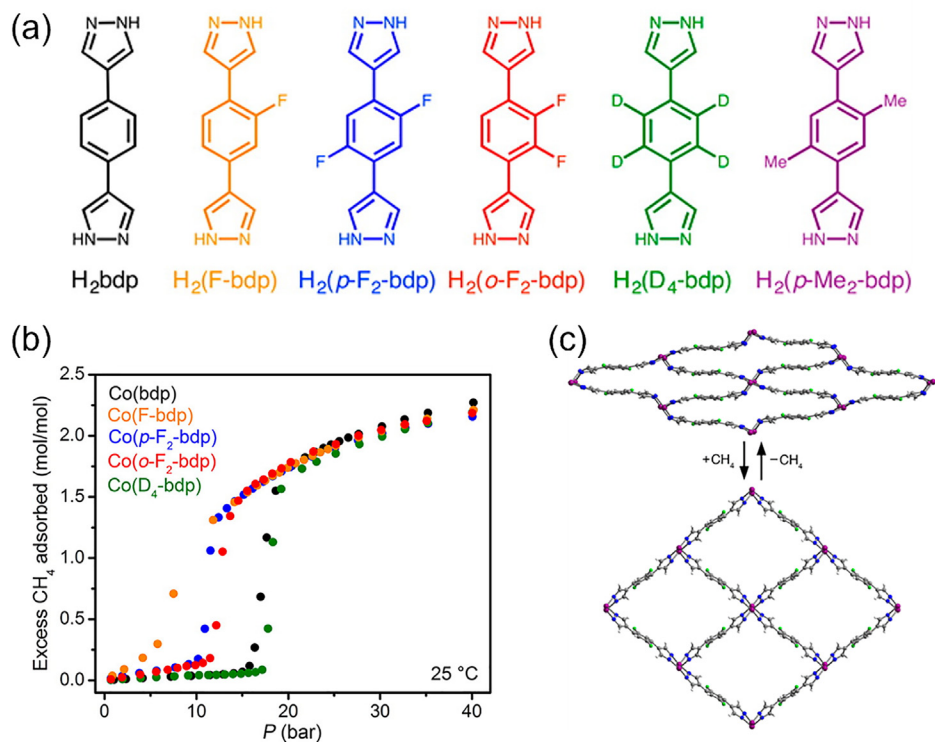


**FIG. 4.** (a) The H<sub>2</sub>bdp derivatives. (b) High-pressure methane uptake isotherms of the Co(bdp) derivatives. (c) Powder x-ray diffraction structures of Co(p-F<sub>2</sub>-bdp) under vacuum (top) and under 20 bar methane (bottom). Reproduced with permission from Alezi *et al.*, *J. Am. Chem. Soc.* **138**, 15019–15026 (2016). Copyright 2016 American Chemical Society.

The introduction of the fluorine groups however destabilizes the collapsed phase, and as shown in Fig. 4(b), the step shifts to lower pressures in the case of Co(F-bdp), Co(p-F<sub>2</sub>-bdp), and Co(o-F<sub>2</sub>-bdp).

In the case of Co(p-F<sub>2</sub>-bdp), the fluorine atoms face the adjacent hydrogen atoms due to the aryl rings ordering in opposite orientation. This leads to a C–H...F–C interaction having the characteristics of a weak hydrogen bond. For the methane uptake isotherm, it was hypothesized that the change in step is caused by a discrete structural phase change from 0 to 20 bar in which the framework expands by 103% in unit cell volume, maintaining the lateral C–H...F–C interactions [Fig. 4(c)]. Because of this, the number of edge-to-face  $\pi\cdots\pi$  interactions that need to be broken for the expansion is weakened leading to a lower step of  $\sim 11$  bar for Co(p-F<sub>2</sub>-bdp) and Co(o-F<sub>2</sub>-bdp); and below 8 bar for Co(F-bdp). The monofluorinated derivative has even lower interactions due to reduced fluorine atoms.

Thus, the tuning of the phase change and the pressure step can be easily achieved synthetically by control over the framework functionalities to lead us to optimal frameworks for on-board applications.

## B. Square pillared materials

[Cu(dhbc)(4,4'-bpy)] (Hdhbc = 2,5-dihydroxybenzoic acid) was the first example of the flexible coordination polymers with the hysteretic adsorption of supercritical N<sub>2</sub> at high pressures and ambient conditions [Fig. 5(a)]. The adsorption isotherm displayed no adsorption at the low-pressure region for the dehydrated framework, followed by the gate opening at 50 bar upon adsorption and the gate closing at 30 bar upon desorption. Different supercritical gases such as CO<sub>2</sub>, O<sub>2</sub>, and CH<sub>4</sub> also displayed similar behaviors with different gate opening

pressures [Fig. 5(b)]. The structural transformations triggered by these gases are facilitated by the framework flexibility arising from the displacement of  $\pi\cdots\pi$  stacked moieties. Although the methane uptake reached only 80 cm<sup>3</sup> g<sup>-1</sup>, this work by Kitagawa *et al.*<sup>29</sup> opened up the new avenues for the flexible frameworks.

Seki<sup>30</sup> observed the methane-induced gate opening at 25 °C for interpenetrated [Cu<sub>2</sub>(bdc)<sub>2</sub>(4,4'-bpy)] (H<sub>2</sub>bdc = terephthalic acid) just below 10 bar and closing of the hysteresis loop at 1 bar. The maximum uptake capacity was 80 cm<sup>3</sup> g<sup>-1</sup> at 25 bar (Fig. 6). At 5 °C, the material displayed an uptake of 90 cm<sup>3</sup> g<sup>-1</sup>, and as expected, the uptake decreased with an increase in pressure. The change in the phase takes place due to change in the style of the interpenetration, which enlarges the pore.

Kaneko *et al.*<sup>31</sup> explored the clathrate formation-mediated adsorption of methane on the latent porous crystal [Cu(4,4'-bipyridine)<sub>2</sub>(BF<sub>4</sub>)<sub>2</sub>]. The high-pressure adsorption isotherms at 258, 273, and 303 K showed the gate opening/closing behavior. At 65 bar and 30 °C, a maximum methane uptake of 60 mg g<sup>-1</sup> was observed (Fig. 7). A linear relationship between log of the gate opening pressure and inverse of the measurement temperature was established. The obtained enthalpy of formation of the clathrate was 13 kJ mol<sup>-1</sup>, and the corresponding dissociation enthalpy was 12.5 kJ mol<sup>-1</sup>. The effect of the measured temperature jump upon adsorption supported the clathrate formation mechanism.

## C. MIL-53 series

The “breathing” behavior upon gas adsorption has been widely observed in different variants of the MIL-53(M) (M = Cr, Al, and Fe)

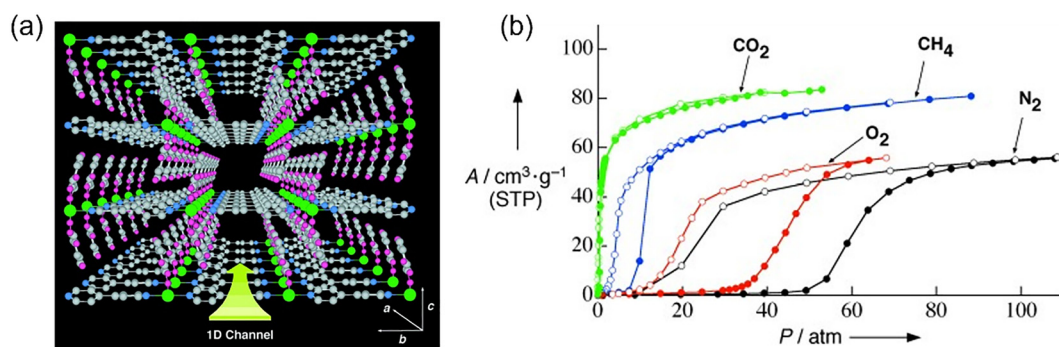


FIG. 5. (a) 3D  $\pi$ -stacked pillared layer structure of the framework and (b) high-pressure gas adsorption isotherms. Reproduced with permission from Kitaura *et al.*, *Angew. Chem., Int. Ed.* **42**, 428–431 (2003) Copyright 2003 John Wiley and Sons.

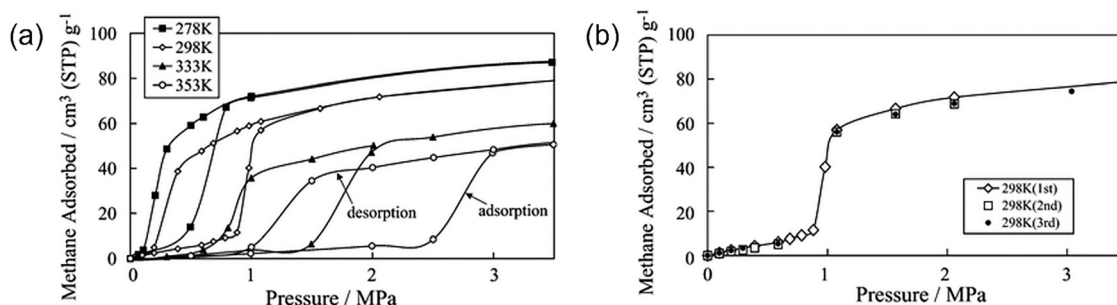


FIG. 6. High-pressure methane adsorption-desorption isotherms of  $[\text{Cu}_2(\text{bdc})_2(4,4'\text{-bpy})]$ . (a) Temperature dependence. (b) Cyclic characteristics of methane adsorption. Reproduced with permission from K. Seki, *Phys. Chem. Chem. Phys.* **4**, 1968–1971 (2002). Copyright 2002 Royal Society of Chemistry.

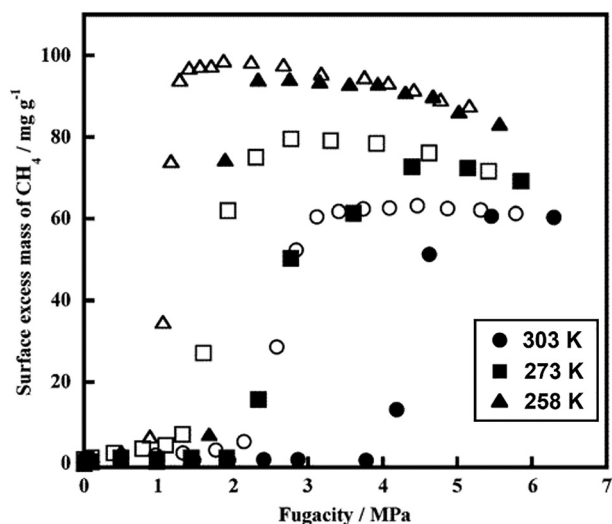
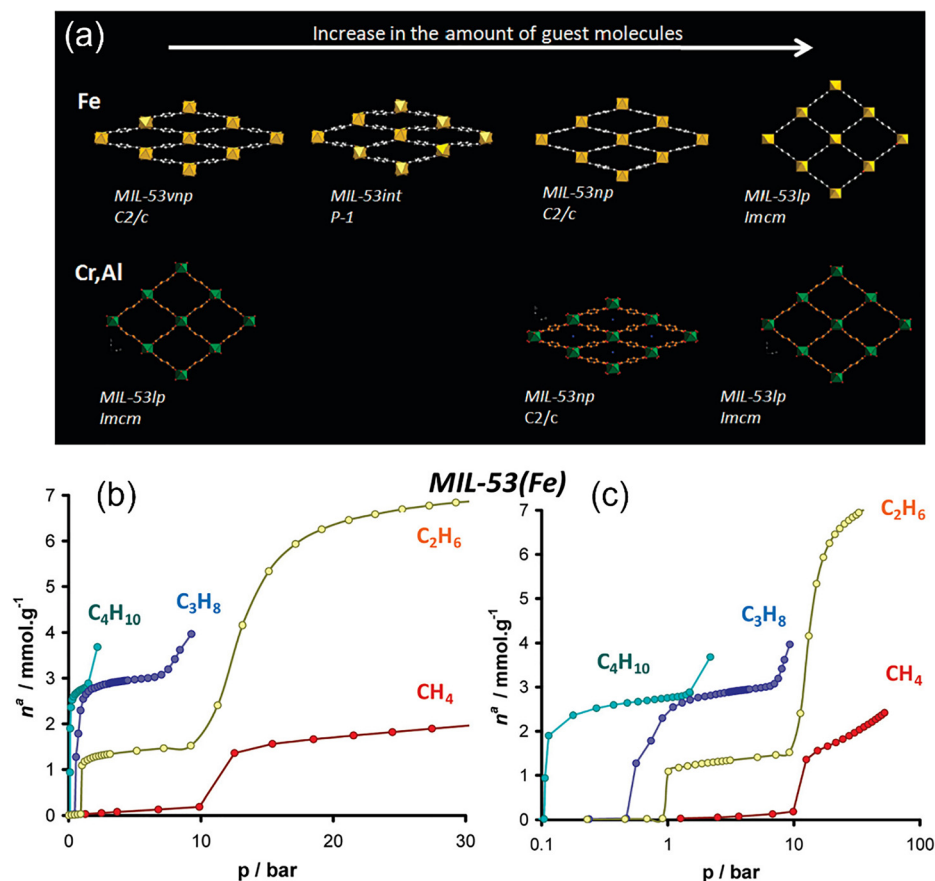


FIG. 7. High-pressure adsorption isotherms of methane on  $[\text{Cu}(4,4'\text{-bipyridine})_2(\text{BF}_4)_2]$ : (●) 303 K (■) 273 K, and (▲) 258 K. Reproduced with permission from Noguchi *et al.*, *J. Phys. Chem. B* **109**, 13851–13853 (2005). Copyright 2005 American Chemical Society.

series (MIL = Materials from Institut Lavoisier).<sup>32</sup> These MOFs are synthesized by combining metal ions in the 3+ oxidation state with 1,4-benzenedicarboxylate linkers to form a three-dimensional structure with one-dimensional channels along the *c*-axis. They can exist in different forms depending on the gas that is adsorbed into the channels. While MIL-53(Cr) and MIL-53(Al) can exhibit either a narrow pore (np) or large pore (lp) structure, the Fe analogue can exist in an additional two structures: a very narrow pore (vnp) form and an intermediate (int) form [Fig. 8(a)]. Therefore, the breathing behavior of MIL-53(Fe) is more complex than both the Cr and Al variants.

The adsorption behavior of methane (and other hydrocarbons) in MIL-53(Fe) was studied in detail by Llewellyn *et al.* through a combination of gas adsorption measurements, microcalorimetry, *in situ* powder x-ray diffraction measurements, and molecular simulations. It was discovered that MIL-53(Fe) undergoes the following phase transitions upon increasing gas uptake: vnp  $\rightarrow$  int  $\rightarrow$  np  $\rightarrow$  lp. At 303 K, MIL-53(Fe) adsorbed negligible amounts of methane at pressures lower than 10 bar [Figs. 8(b) and 8(c)]. After 10 bar, however, the methane uptake within the material suddenly increases to around  $1.4 \text{ mmol g}^{-1}$ . This likely indicates the transition of MIL-53(Fe) to the int form as suggested by PXRD studies performed on the material after  $\text{CH}_4$  adsorption at different pressures.



**FIG. 8.** (a) The evolution of different structures of MIL-53(M) (M = Cr, Al, and Fe) upon increasing adsorbate uptake. (b) and (c) Adsorption isotherms (standard plot and semilog plot) for various gases (methane = red,  $\text{C}_2\text{H}_6$  = green,  $\text{C}_3\text{H}_8$  = blue, and  $\text{C}_4\text{H}_{10}$  = cyan) in MIL-53(Fe) at 303 K. Reproduced with permission from Llewellyn *et al.*, J. Am. Chem. Soc. **131**, 13002–13008 (2009). Copyright 2009 American Chemical Society.

This indicates that MIL-53(Fe) progressively goes through several structural transitions upon methane adsorption before finally transforming into the lp form at higher pressures. On the other hand, methane adsorption measurements in MIL-53(Cr) MIL-53(Al) revealed type I isotherms, implying that these analogues do not undergo the same structural transitions as those for MIL-53(Fe) upon increasing uptake.

In 2009, a variant of MIL-53(Al) was synthesized to contain an amino group on the linker.<sup>33</sup> This MOF, known as MIL-53(Al)- $\text{NH}_2$ , exhibits a topology that is similar to that for the original MIL-53(M) analogues. The structures of different forms for this MOF also correspond to those for the non-functionalized systems. Couck *et al.* measured the methane adsorption properties for this analogue when the authors investigated the material for its ability to separate  $\text{CO}_2$  to  $\text{CH}_4$ .<sup>34</sup> While MIL-53(Al) adsorbed significant amounts of methane at 303 K and low pressures, MIL-53(Al)- $\text{NH}_2$  did not display any noticeable uptake at pressures lower than 2 bar. The authors attributed this behavior to the reduced number of nonpolar binding sites for methane as a result of the presence of amino groups on the aromatic rings of the linker. As the pressure increases, the methane uptake in MIL-53(Al)- $\text{NH}_2$  increases weakly and almost linearly to a capacity of around  $2.4 \text{ mmol g}^{-1}$  at 30 bar.

The shape of the methane adsorption isotherm for MIL-53(Al)- $\text{NH}_2$  at temperatures near 298 K also suggests a breathing phenomenon

that is similar to that observed for MIL-53(Fe). The presence of  $\text{N}-\text{H}\cdots\text{O}$  hydrogen bonding interactions between the amino groups, and the  $[\text{AlO}_6]$  chains could help stabilize the vnp and np phases of the framework.<sup>26</sup> Bolinois *et al.* verified this by performing methane adsorption measurements in this material at different temperatures and high pressures. Figure 9 shows the total gravimetric methane adsorption isotherms that were collected for MIL-53(Al)- $\text{NH}_2$  at 298 K and up to different pressures.

Overall, two phase transitions can be observed for the material upon methane adsorption. The plateau in the methane uptake at pressures lower than 20 bar suggests that the MOF exists in the vnp structure. After 20 bar, the isotherm exhibits a sudden jump in the uptake, which indicates that the material transitions to the np form. The methane uptakes are nearly constant within the range of 20–45 bar, implying that MIL-53(Al)- $\text{NH}_2$  stays in the np structure in this region. Another increase in uptake can be observed after 50 bar, which represents a transition to the lp structure. The authors observed that the corresponding transition pressures decrease with decreasing temperature, with a relatively faster rate of the  $\text{np} \rightarrow \text{lp}$  transition.

The 5.8–35 and 5.8–65 bar gravimetric methane working capacities for MIL-53(Al)- $\text{NH}_2$  were measured to be  $74$  and  $115 \text{ cm}^3 \text{ g}^{-1}$ , respectively. As a comparison, MIL-53(Al) exhibits a 5.8–65 bar working capacity of  $133 \text{ cm}^3 \text{ g}^{-1}$ . However, if MIL-53(Al)- $\text{NH}_2$  is first pressurized by methane at 120 bar to ensure a complete transition to



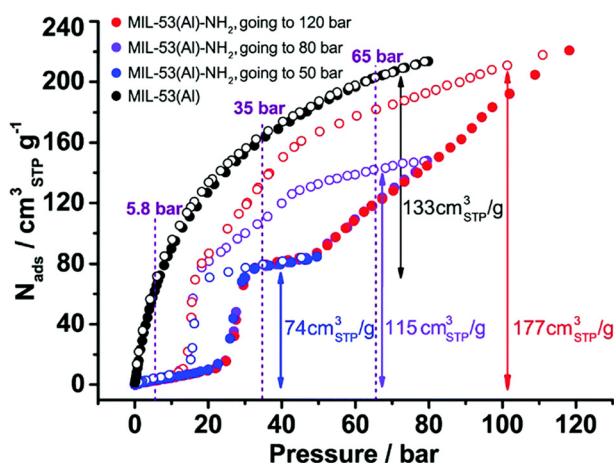


**FIG. 9.** Total gravimetric methane adsorption isotherms in MIL-53(Al) (black) and MIL-53(Al)-NH<sub>2</sub> (blue = up to 50 bar, violet = up to 80 bar, and red = up to 120 bar) at 298 K and high pressures (adsorption = closed circles and desorption = open circles). The black arrow indicates the 5.8–65 bar working capacity for MIL-53(Al), while the blue, violet, and red arrows represent 5.8–35, 5.8–65, and 5.8–100 bar (after being pressurized to 120 bar) working capacities, respectively, for MIL-53(Al)-NH<sub>2</sub>. Reproduced with permission Bolinois *et al.*, *Chem. Commun.* **53**, 8118–8121 (2017). Copyright 2017 Royal Society of Chemistry.

the lp phase and then brought back down to 65 bar, the 5.8–65 bar working capacity becomes  $177 \text{ cm}^3 \text{ g}^{-1}$ . Therefore, even though the total methane uptake for MIL-53(Al)-NH<sub>2</sub> is lower than that for MIL-53(Al) across the considered pressure range, it exhibits a higher 5.8–65 bar working capacity due to triggering of the lp phase at higher pressures. Although this strategy could be beneficial to achieve good methane storage performance, the complete lp phase transition requires extremely high pressures ( $>120$  bar). Bolinois *et al.* also investigated the methane adsorption properties of MIL-53(Al) with different ratios of BDC/BDC-NH<sub>2</sub> mixed linkers at 298 K and high pressures to see whether the np  $\rightarrow$  lp phase transition can be triggered at lower pressures. It was discovered that the np to lp transition pressure can indeed be lowered by reducing the abundance of the amino group on the BDC linkers.

Kundu *et al.* reported additional variants of MIL-53(Al) by introducing different numbers of -OH groups on the BDC linkers.<sup>22</sup> Particularly, the authors synthesized MIL-53(Al)-OH and MIL-53(Al)-(OH)<sub>2</sub> by combining Al<sup>3+</sup> ions with 2-hydroxyterephthalate and 2,5-dihydroxyterephthalate linkers, respectively (Fig. 10). The crystal structures of both MOFs display  $\pi \cdots \pi$  stacking of the BDC-OH linkers, which results in stabilization of the vnp phase. Figure 11 shows the total volumetric methane adsorption isotherms in both analogues at different temperatures and high pressures. A large hysteresis can be observed in the adsorption isotherms for MIL-53(Al)-OH at all temperatures, which indicates gate-opening closure caused by depressurization [Fig. 11(a)].

The presence of two steps in the isotherm at 273 K represents three distinct phases for MIL-53(Al)-OH (vnp, np, and lp). The MOF displays negligible methane uptake at pressures lower than 8 bar, which implies stability of the vnp phase up to this pressure. The presence of the np phase of the material can be observed within the region of 14–17 bar, and a further increase in pressure leads to expansion to

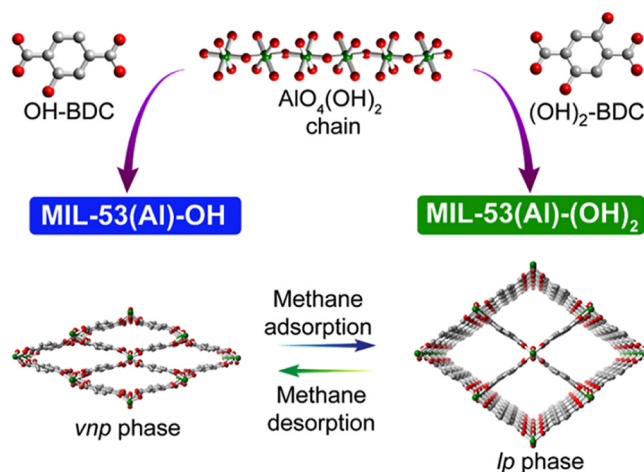


**FIG. 10.** Scheme illustrating the synthesis of MIL-53(Al)-OH and MIL-53(Al)-(OH)<sub>2</sub> as well as the phases of the MOFs exhibit upon methane adsorption and desorption. Reproduced with permission from Kundu *et al.*, *Chem. Mater.* **31**, 2842–2847 (2019). Copyright 2019 American Chemical Society.

the lp phase. During desorption, the lp  $\rightarrow$  np transition was not observed as the MOF transitions back to the vnp phase at pressures below 3.3 bar. The methane adsorption isotherm for MIL-53(Al)-(OH)<sub>2</sub> at 273 K does not show the distinct plateau that is representative of the np phase [Fig. 11(b)]. Instead, the vnp phase for this MOF gradually transitions into the lp phase at a pressure above 30 bar during adsorption and the structure transforms back into the vnp phase at pressures below 2.7 bar during desorption.

The methane adsorption isotherm for MIL-53(Al)-OH at 298 K reveals a vnp  $\rightarrow$  lp transition at a pressure above 15 bar, whereas the reverse transition occurs below 4.1 bar. On the other hand, the isotherm for MIL-53(Al)-(OH)<sub>2</sub> at this temperature displays the gate-opening effect above 46 bar and undergoes gate closure below 5.8 bar. The authors attributed the difference in gate-opening pressures between MIL-53(Al)-OH and MIL-53(Al)-(OH)<sub>2</sub> to the efficient  $\pi \cdots \pi$  stacking and dual hydrogen bonding interactions between the 2,5-dihydroxyterephthalate linkers and the bridging -OH groups in the latter. This results in a greater stability of the vnp phase for this variant. The 5.8–35 and 5.8–65 bar volumetric methane working capacities for MIL-53(Al)-OH at 298 K were measured to be 114 and  $164 \text{ cm}^3 \text{ cm}^{-3}$ , respectively, with the latter being comparable to that for the top-performing MOFs for this definition of the working capacity.

The corresponding working capacities for MIL-53(Al)-(OH)<sub>2</sub> are lower than those for MIL-53(Al)-OH since the structure exists predominantly in the vnp phase until the pressure is greater than 46 bar. Indeed, the incomplete np  $\rightarrow$  lp phase transition for MIL-53(Al)-(OH)<sub>2</sub> at 65 bar diminishes the working 5.8–65 bar working capacity for this material.

Kundu *et al.* also published a study in 2019 in which they synthesized MIL-53(Al)-OH and MIL-53(Al)-NH<sub>2</sub> using different H<sub>2</sub>O/DMF (DMF = N,N'-dimethylformamide) ratios.<sup>26(e)</sup> It was discovered that using a higher concentration of DMF increases the stability of the lp phases (since the MOF particle size consequently decreases), with the np  $\rightarrow$  lp phase transitions occurring at lower pressures. This generally resulted in both higher methane uptake and 5.8–65 bar working

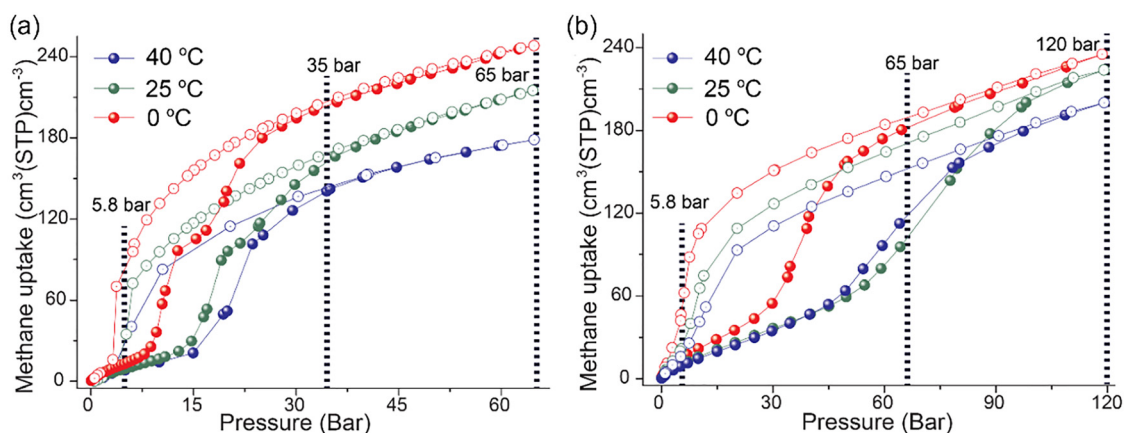


**FIG. 11.** Total volumetric methane adsorption isotherms in (a) MIL-53(Al)-OH and (b) MIL-53(Al)-(OH)<sub>2</sub> at 273 K (red), 298 K (green), and 313 K (blue) and high pressures (adsorption = closed circles and desorption = open circles). Reproduced with permission from Kundu *et al.*, *Chem. Mater.* **31**, 2842–2847 (2019). Copyright 2019 American Chemical Society.

capacities compared to using samples that were synthesized using lower DMF concentrations. Nevertheless, it was observed that using a DMF concentration of 20% in the synthesis of MIL-53(Al)-NH<sub>2</sub> resulted in a *ca.* 33% increase in the 5.8–65 bar gravimetric working capacity compared to using 0% DMF. Interestingly, a further increase in the DMF concentration (> 40%) for this variant resulted in a gradual decrease in the working capacities due to the dominant effect of the retained amounts over the uptake capacity.

#### D. X-dia-1-Ni

In 2018, Yang *et al.* synthesized a flexible MOF exhibiting dia topology and sixfold interpenetration by combining Ni<sup>2+</sup> ions with 4-(4-pyridyl)-biphenyl-4-carboxylate linkers (Fig. 12).<sup>35</sup> This MOF, denoted X-dia-1-Ni, is present as a non-porous phase after activation, but undergoes several phase transitions upon CO<sub>2</sub> adsorption at 195 K. This MOF was also evaluated for methane adsorption at 298 K and high pressures and was found to display a S-shaped isotherm

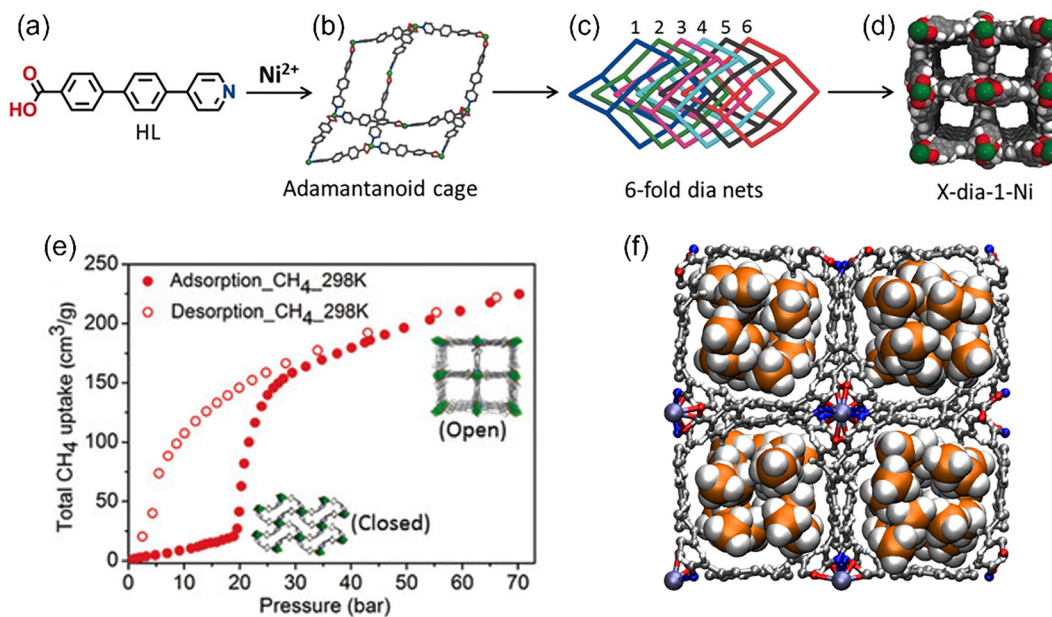


**FIG. 12.** Scheme illustrating the synthesis of X-dia-1-Ni. (a) 4-(4-pyridyl)-biphenyl-4-carboxylic acid ligand, (b) adamantanoid cage and (c) sixfold interpenetrated net of X-dia-1-Ni, and (d) view of the rectangular channels of the MOF along the *c*-axis. (e) Total gravimetric methane adsorption isotherm in X-dia-1-Ni at 298 K and high pressures (adsorption = closed circles and desorption = open circles). A crystallographic density of 0.852 g cm<sup>3</sup> cm<sup>-3</sup> can be used to convert the gravimetric uptakes to volumetric units for the open structure. (f) Modeled structure of X-dia-1-Ni with methane localized in the material at high pressures. Atom colors: C(MOF) = gray, C(methane) = orange, H = white, N = blue, O = red, and Ni = lavender. Reproduced with permission from Yang *et al.*, *Angew. Chem., Int. Ed.* **57**, 5684–5689 (2018). Copyright 2018 Wiley-VCH (Germany).

upon adsorption of the gas. Notably, X-dia-1-Ni adsorbed minimal quantities of methane below the phase change pressure of 20 bar before exhibiting a significant increase in uptake upon switching to a fully open phase [Fig. 12(e)].

The total volumetric methane uptake at 298 K was measured to be 150 and 189  $\text{cm}^3 \text{cm}^{-3}$  at 35 and 65 bar, respectively. The potential 5–35 bar working capacity for X-dia-1-Ni, as calculated from the difference in uptakes between 5 and 35 bar in the adsorption isotherm, is 147  $\text{cm}^3 \text{cm}^{-3}$ . However, the presence of hysteresis in the desorption isotherm reduces the 5–35 bar and 5–65 bar working capacities to 110 and 149  $\text{cm}^3 \text{cm}^{-3}$ , respectively. Simulations of methane adsorption in the fully open phase of X-dia-1-Ni reveal that the methane molecules essentially localize within the pores of the material at high pressures [Fig. 12(f)]. The calculated uptakes at 298 K/35 bar and 298 K/65 bar were in good agreement with experiment.

Although there are other MOFs with the same topology that were studied for methane adsorption,<sup>36</sup> X-dia-1-Ni was the only flexible dia MOF that was investigated for this application to the best of our knowledge.

### E. DUT-49

In 2012, Stoeck *et al.* synthesized a carbazole-based MOF that exhibited exceptionally high methane uptake at 298 K and high pressures.<sup>37</sup> This MOF, known as DUT-49 (Dresden University of Technology No. 49), consists of  $\text{Cu}^{2+}$  ions coordinated to 9,9'-([1,1'-biphenyl]-4,4'-diyl)bis(9H-carbazole-3,6-dicarboxylate) (BBCDC) linkers. The MOF possesses a very high specific surface area of 5476  $\text{m}^2 \text{g}^{-1}$  and a large total pore volume of 2.91  $\text{cm}^3 \text{g}^{-1}$ . This allowed the material to exhibit excellent  $\text{H}_2$ ,  $\text{CO}_2$ , and methane adsorption properties at high pressures. Indeed, experimental measurements revealed that DUT-49 displayed an excess gravimetric methane uptake of 291  $\text{mg g}^{-1}$  at 298 K/80 bar and a total volumetric uptake of 236  $\text{cm}^3 \text{cm}^{-3}$  at 298 K/110 bar (Fig. 13). The maximum methane uptake capacity for this MOF was the highest out of all porous materials at the time.

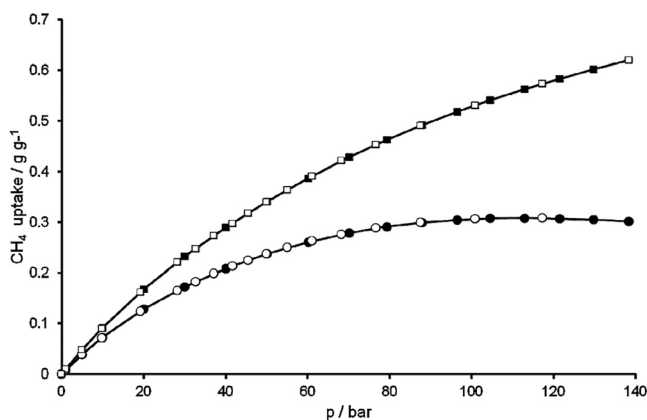


**FIG. 13.** Excess (circles) and total (squares) gravimetric methane adsorption isotherms in DUT-49 at 298 K and high pressures (adsorption = closed symbols and desorption = open symbols). A crystallographic density of 0.437  $\text{g cm}^3 \text{cm}^{-3}$  can be used to convert the gravimetric uptakes to volumetric units. Reproduced with permission from Stoeck *et al.*, Chem. Commun. **48**, 10841–10843 (2012). Copyright 2012 Royal Society of Chemistry.

In 2016, it was revealed that DUT-49 displayed negative gas adsorption for methane at low temperatures in which the uptake decreased slightly at a certain pressure before increasing again.<sup>38</sup> Figure 14 shows the experimentally measured adsorption and desorption isotherms for methane in the material at 111 K and low pressures. A sudden drop in methane uptake can be observed in the adsorption isotherm at *ca.* 10 kPa. In order to gain insight into this phenomenon, the authors performed *in situ* PXRD measurements during methane adsorption in the material at low temperatures. It was discovered that DUT-49 exists as an open-pore structure (denoted DUT-49*op*) at low pressures before transitioning to a closed-pore form (denoted DUT-49*cp*) at the step where the methane uptake suddenly decreases in the isotherm.

A molecular illustration of both structures as determined through *in situ* PXRD is shown in Fig. 15. As the pressure increases, the structure transitions back to the open-pore structure as the pores become filled with methane molecules, thus indicating that this initial transformation is reversible.

The contraction of DUT-49*op* is attributed to the concerted rotation of metal–organic polyhedra around the [111] axis, which in turn led to a notable deformation of the BBCDC linkers. However, the connectivity of the framework was still preserved during the transition and the porosity within the different cages of the MOF was only slightly affected. The authors showed through density functional theory (DFT) calculations that DUT-49*op* is more stable than DUT-49*cp* by 91  $\text{kJ mol}^{-1}$  per linker (Fig. 15). Upon methane adsorption, however, this energy difference was overcome by the higher affinity of the adsorbate to the closed-pore structure since the methane molecules can interact more strongly with the framework in a confined environment. This resulted in a higher adsorption enthalpy ( $\Delta H$ ) for methane toward DUT-49*cp* relative to DUT-49*op*, with a value that is comparable in magnitude to that for the energy ( $\Delta E$ ) of the structural transition per linker. This suggests that the adsorption of methane compensates for the energy penalty for the transition of the open-pore structure to the closed-pore structure.

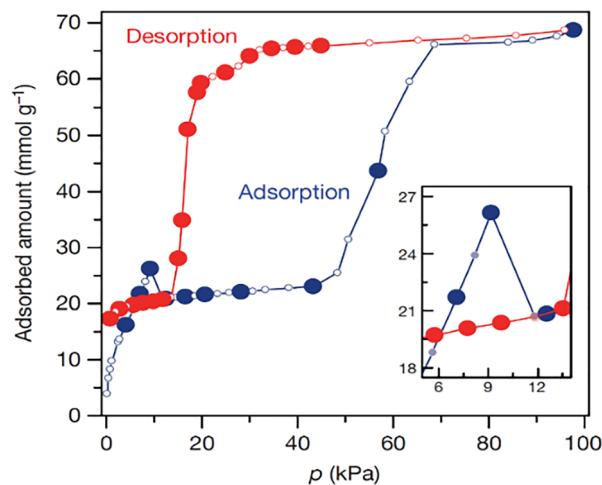


**FIG. 14.** Methane adsorption and desorption isotherms in DUT-49 at 111 K and low pressures (adsorption = blue and desorption = red). The inset shows the pressure region in which negative gas adsorption occurs. Reproduced with permission from Krause *et al.*, Nature **532**, 348–352 (2016). Copyright 2016 Springer Nature.

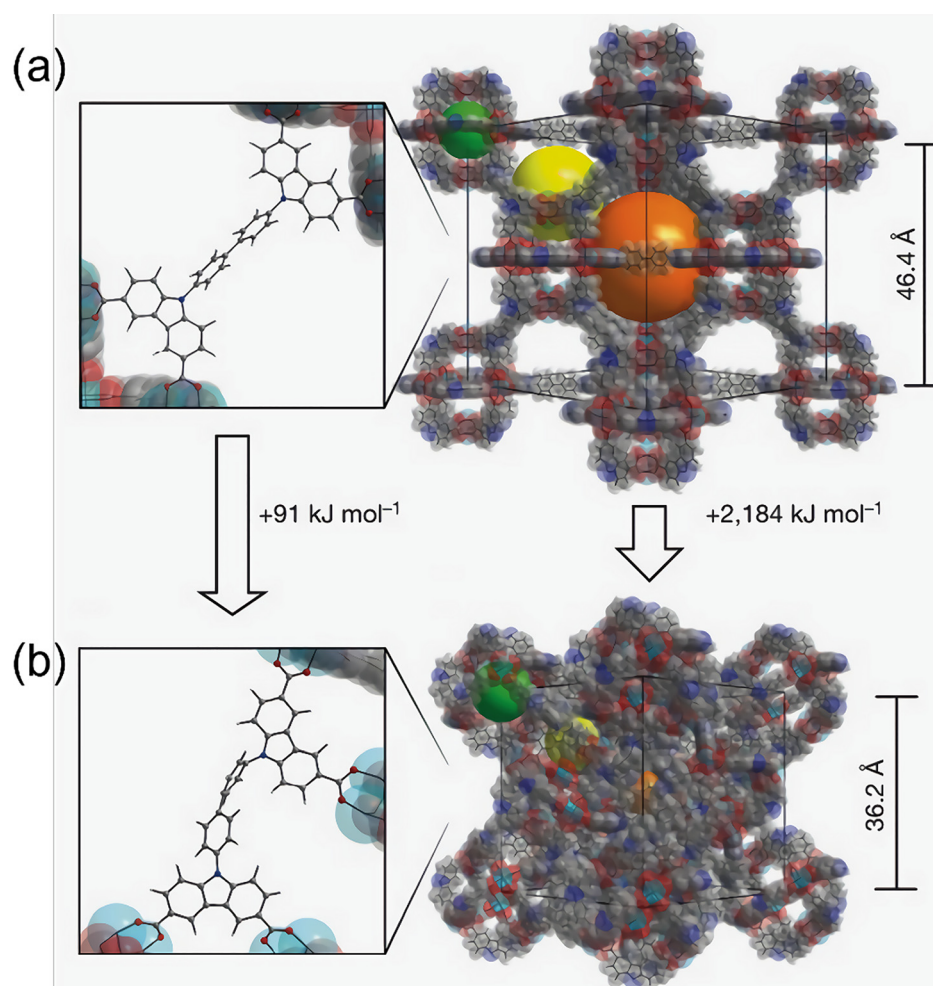


**FIG. 15.** Orientation of the BBCDC linker (left) and view of the crystal structure along the [110] axis (right) for (a) DUT-49<sup>op</sup> and (b) DUT-49<sup>cp</sup>. The energy values correspond to the relative energies between the two structures for a single linker (left) and the entire unit cell (right) as determined from DFT calculations. Reproduced with permission from Krause *et al.*, Nature **532**, 348–352 (2016). Copyright 2016 Springer Nature.

Interestingly, the authors observed that DUT-49<sup>op</sup> transitions to an intermediate-pore structure (denoted DUT-49<sup>ip</sup>) upon the desorption of methane at 111 K, thereby explaining the wide hysteresis. The structure transitions into DUT-49<sup>cp</sup> at pressures lower than 20 kPa, but does not switch back to DUT-49<sup>op</sup>. Nevertheless, the open-pore structure can be regenerated by heating the material from 111 to 298 K at constant pressure. Overall, Krause *et al.* showed that the negative gas adsorption in DUT-49 at low temperatures is attributed to the sudden hysteretic structural deformation and pore contraction of the MOF, which causes the spontaneous release of methane molecules. This is the only report of this unusual adsorption behavior to the best of our knowledge. Subsequent theoretical studies by Evans *et al.* confirmed that the negative gas adsorption in DUT-49 originates from molecular buckling of the BBCDC linkers, which in turn allowed for a large-scale structural transformation of the entire framework.<sup>39</sup>

Krause *et al.* had recently investigated the effects of temperature on CH<sub>4</sub> and other gases in DUT-49.<sup>40</sup> It was observed that as the temperature increases, the transition region is shifted to higher pressures, which in turn results in an enhancement of the amount of gas released upon negative gas adsorption. Furthermore, the same research group synthesized different variants of DUT-49 by tuning the length of the

ligand and studied how this affected the negative gas adsorption transitions of CH<sub>4</sub>.<sup>41,42</sup> It was revealed through a combined experimental and theoretical analysis that elongation of the linker reduces the stress required to stimulate structural contraction.

### III. FLEXIBLE CONSTITUENTS

In addition to the large-scale flexations involved in breathing phenomena, MOFs can undergo dynamic motions of constituent functional groups inside otherwise rigid MOF scaffolds. This regional mobility can take the form of rotations of moieties or ligands and conformational alterations of dangling side chains or pendant groups.

Regional mobility can result in the same dramatic stepwise sorption isotherms typically observed in the isotherms of fully flexible materials, as they can act as gate opening effects in the same manner. These systems enjoy the same advantages for sorption applications as their fully flexible counterparts, that is, the very low uptakes prior to gate opening and resulting in high working capacities. It should be noted, however, that no structures exhibiting this behavior in response to methane sorption have currently been reported to the best of our knowledge.

More typically, the effects of regional mobility are subtle. In such structures, mobile elements are uncoordinated to their counterparts and flex in response to stimulation gradually and independently of their counterparts resulting in type I isotherms. This can be the result of more gradual gate-opening effect or conformational shifting to maximize surface area, cell volume, and/or host-guest interaction. Due to the lack of clear phase shifting thresholds, these effects are often not initially obvious and require specific investigation, typically through theoretical modeling to elucidate the mechanisms at work. While not visibly dramatic, these subtle effects can, nevertheless, have a significant impact on sorption uptakes.<sup>15</sup>

As these systems lack a stepwise isotherm, they do not have the advantage of extremely low uptakes observed of the closed pore structures seen at low pressures to enhance working capacity in the way fully flexible and gate-opening regionally mobile MOFs do. These structures, however, take advantage of responsive (typically to sorption uptake) behavior to maximize loading in a way that rigid analogues cannot, occasionally resulting in significant increases in uptake at higher pressures. As such, these systems have potential for the same methane uptake applications as their fully flexible counterparts.

### A. Conformational adjustment

The inclusion of mobile moieties in otherwise rigid structures can, in response to incoming sorbate molecules, cause structural alterations to further accommodate sorption in the form of increasing surface area exposure and maximizing pore volume accessibility.

In 2014, Li *et al.* synthesized UTSA-76a (University of Texas San Antonio No. 76 activated), a MOF exhibiting one of the highest reported working capacities to date and a significant example of this effect.<sup>20</sup> Created as an isostructural analogue of the rigid NOTT-101a,<sup>43</sup> both crystals are composed of copper paddle-wheels jointing tetracarboxylic isophthalate linkers with UTSA-76a including pyrimidine functionality in place of the benzene moieties of the parent structure [Figs. 16(a) and 16(b)].

Owing to similarities in lattice parameters (differing by  $\sim 1.2\%$ ), surface areas ( $2820$  and  $2805 \text{ m}^2 \text{ g}^{-1}$  for UTSA-76a and NOTT-101a, respectively) and pore volumes ( $1.09$  and  $1.08 \text{ cm}^3 \text{ g}^{-1}$ ), both crystals exhibited nearly identical high pressure methane uptakes at  $125$  and  $150 \text{ K}$  and type I isotherms. Isotherms at  $298 \text{ K}$ , however, diverged with UTSA-76 found to have significantly higher uptake. At

$65 \text{ bar}$ , the parent structure had a volumetric uptake of  $237 \text{ cm}^3 \text{ cm}^{-3}$ , which increased to  $257 \text{ cm}^3 \text{ cm}^{-3}$  in UTSA-76a [Fig. 16(c)]. The resultant working capacity in the latter structure was  $197 \text{ cm}^3 \text{ cm}^{-3}$ .

Computational first-principles examination of methane loading in NOTT-101a and UTSA-76a was undertaken using dispersion corrected density functional theory.<sup>43</sup> The structures exhibited similar initial sorption onto the open metals and in the cage windows, which is typically sorptive behavior in copper paddlewheel MOFs. Surprisingly, tertiary sorption onto the linker bodies, in the vicinity of the variant functionality, was found to be nearly identical in site location and interaction energies for the two variants. This indicates that the greater electronegativity of the pyrimidine rings is not the motivating factor of the increased uptake. Without an obvious difference in intermolecular interaction energetics, the potential mobility of the pyrimidine/benzene groups in the two analogues was considered.

The barrier of rotation was calculated, and it was found that the pyrimidine rotational energy barrier is less than half that of its benzene counterpart [Fig. 16(d)] indicating a much more facile response to sorptive stimuli. This accounts for the similar behavior of the two variants at lower temperatures and pressures, under which conditions ring rotation is less likely to be successfully induced or to have as significant an effect on uptakes. This finding is also consistent with the higher uptake of the pyrimidine variant at  $298 \text{ K}$  and saturation conditions, where the high temperature and increase in host-sorbate and sorbate-sorbate interactions make the likelihood of the induction of ring rotations and the value of optimized pore surface/shapes significant.

Further examination of the structures was undertaken to experimentally verify the computational result. Elastic neutron scattering, graphing intensity vs temperature, illustrated that small timescale pyrimidine rotation in UTSA-76a took place at approximately  $70 \text{ K}$ , while similar motions of the NOTT-101a benzene ring were not observed until temperatures of  $150 \text{ K}$  were applied. This confirmed a more facile rotational motion of the pyrimidine ring in UTSA-76a in comparison with the benzene in the parent structure and illustrates the potentially large effect of small-scale localized motions in otherwise rigid MOF scaffolds.

### B. Gate opening effects

The flexation of organic ligands and/or their constituent moieties can be capable of enacting gate opening effects to otherwise

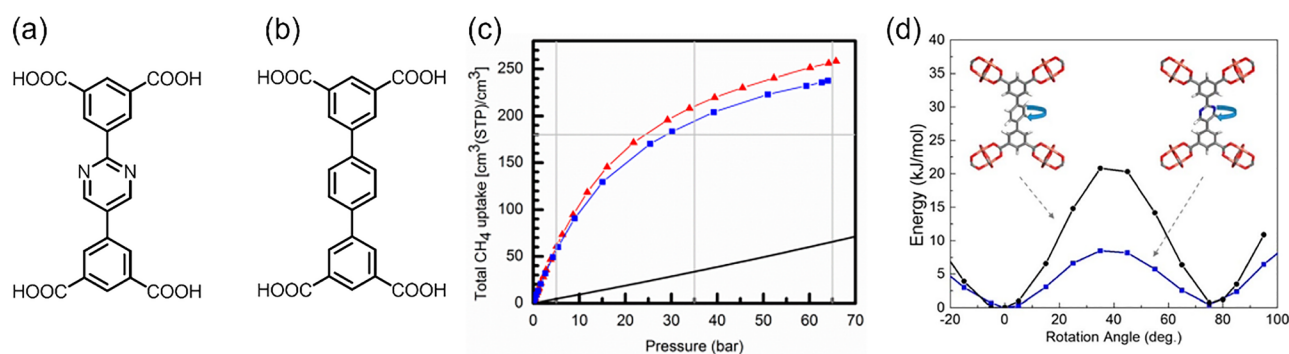


**FIG. 16.** Organic ligands of UTSA-76a (a) and NOTT-101a (b). (c) Methane uptake in UTSA-76a (red), NOTT-101a (blue), and bulk methane (black). (d) Energy changes due to rotation of the central benzene/pyrimidine rings in NOTT-101a (black) and UTSA-76a (blue). Reproduced with permission from Li *et al.*, *J. Am. Chem. Soc.* **136**, 6207–6210 (2014). Copyright 2014 American Chemical Society.

inaccessible pores in rigid scaffolds. Depending on how facile the sorbate response is, this could cause significant differences in uptakes between low pressure and high-pressure isotherms even in systems without discrete phase shifts.

In 2008, Morris *et al.* synthesized ZIF-90 (Zeolitic Imidazolate Framework 90) composed of  $\text{Zn}^{2+}$  ions coordinated to imidazolate-2-carboxyaldehyde linkers forming crystal structures with sodalite topology, a BET surface area of  $1270 \text{ m}^2 \text{ g}^{-1}$ , and cage window diameters of  $3.5 \text{ \AA}$  [Figs. 17(a) and 17(b)].<sup>44</sup> While no high-pressure methane isotherms are known to have been published to date, Grand Canonical Monte Carlo simulations have projected methane uptakes potentially as high as  $\sim 160 \text{ cm}^3 \text{ cm}^{-3}$  at 298 K and 65 atm with working capacities of and  $\sim 120$  and  $\sim 140 \text{ cm}^3 \text{ cm}^{-3}$  at 35 and 65 atm, respectively.<sup>45</sup> As the kinetic diameter of methane is  $3.8 \text{ \AA}$ , in comparison with the  $3.5 \text{ \AA}$  window diameter of ZIF-90, the permeability with respect to methane indicates gate-opening mechanisms at work in this structure. It is well known that many ZIFs undergo small-scale flexations, which permit access by theoretically size excluded sorbate access.<sup>46</sup>

In 2016, Phuong *et al.* undertook the computational examination of ZIF-90 to elucidate the nature of the mechanism permitting methane access to the crystal structure.<sup>47</sup> Using Gibbs Ensemble Monte Carlo (GEMC) modeling correlated with experimental measurements and molecular dynamic (MD) simulations, sorption in a flexible ZIF-90 framework was modeled at various methane loadings. Changes in the size of the pore apertures were found to be a function of loading with higher uptakes inducing a larger population of expanded apertures [Fig. 17(c)]. This confirms the sorbate induced nature of the shifts in channel diameters and opening of the system to methane penetration.

In 2018, Zheng *et al.* reexamined the system with respect to linker mobility.<sup>45</sup> Specifically, two types of flexations were considered. Linker swing defined as the partial rotation of the linker about the Zn–Zn axis, which is to say the gating motion, and rotational orientation of the terminal aldehyde. It was found that swing freedom and aldehyde orientation were correlated, indicating the potential for tuning the gate opening.

While a number of ZIF structures do exhibit pore flexibility as discussed above, the usefulness of this in comparison with a fully rigid structure is not apparent. Though permitting access to otherwise inaccessible pores, there is little evidence that these subtle gate openings

result in higher uptakes than comparable rigid structure with naturally larger pore apertures.

More pronounced, and potentially viable, gate opening phenomena can be observed in the  $\text{M}(\text{bim})_2$  series of structures, composed of benzimidazolate linkers joined by divalent metal ions in a sodalite topology.

The  $\text{Zn}^{2+}$  and  $\text{Co}^{2+}$  analogues, also known as ZIF-7 and ZIF-9, were synthesized in 2006 by Park *et al.*<sup>46(a)</sup> (though the hydrated  $[\text{Zn}(\text{bim})_2] \cdot (\text{H}_2\text{O})_{1.67}$  structure had also been previously reported<sup>48</sup>). Little measurable variation was observed between the variants in terms of bond lengths and ligand orientations,<sup>46(a)</sup> with  $\text{Zn}(\text{bim})_2$  and  $\text{Co}(\text{bim})_2$  having  $\text{CO}_2$  derived BET surface areas of  $240 \text{ m}^2 \text{ g}^{-1}$  and  $224 \text{ m}^2 \text{ g}^{-1}$ , respectively.<sup>49</sup>

In 2018, McGuirk *et al.* reported stepwise high pressure  $\text{CH}_4$  isotherms for both structures. Volumetric uptakes at 60 bar for the  $\text{Zn}^{2+}$  and  $\text{Co}^{2+}$  analogues were 95 and  $96 \text{ cm}^3 \text{ cm}^{-3}$  [Fig. 18(a)]; a result in line with the high similarity in crystal structures. However, a notable difference between the variants was observed in the phase transition pressure, with  $\text{Zn}(\text{bim})_2$  undergoing structural transformation at  $\sim 10$  bar at 303 K, while  $\text{Co}(\text{bim})_2$  transitions at  $\sim 15$  bar. This result was attributed to the propensity of the open shell  $\text{Co}^{2+}$  ions to engage in ligand to metal  $\pi$ -bonding resulting in higher energy barriers to rotation than these formed by the closed shell  $\text{Zn}^{2+}$  ions.<sup>50</sup>

McGuirk *et al.* also synthesized and examined a third analogue, the cadmium(II) imidazolate framework also known as CdIF-13.<sup>50</sup> This structure, in addition to having longer nitrogen-metal bond lengths, had a distorted sodalite topology, in contrast to its topologically ideal counterparts, and also exhibited significant differences in linker rotational angles.<sup>50</sup>

Negligible  $\text{CH}_4$  sorption was observed for  $\text{Cd}(\text{bim})_2$  for pressures reaching 80 bar at 303 K. Reducing the temperature down to 273 K, however, produces a similar stepwise isotherm to those observed for the  $\text{Zn}^{2+}$  and  $\text{Co}^{2+}$  analogues with the phase transition at 45 bar and a loading capacity of 138 v/v at 65 bar [Fig. 18(b)]. The more extreme conditions needed to induce gate-opening were hypothesized to derive from the greater flexibility of the elongated bonds allowing for a more stable initial state.<sup>50</sup>

Though loaded closed-pore structures have not yet been achieved in wet lab experimentation for the  $\text{Zn}^{2+}$  and  $\text{Co}^{2+}$  analogues, a

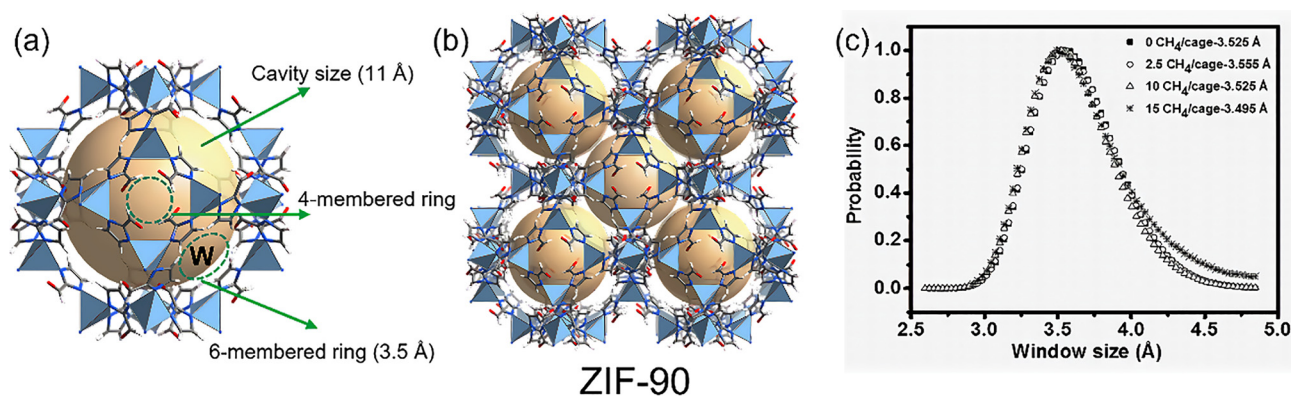


**FIG. 17.** ZIF-90 single cell (a) and  $2 \times 2 \times 2$  system (b). (c) Change in the size of pore aperture as a function of methane loading. Reproduced with permission from Phuong *et al.*, *Microporous Mesoporous Mater.* **235**, 69–77 (2016). Copyright 2016 Elsevier.

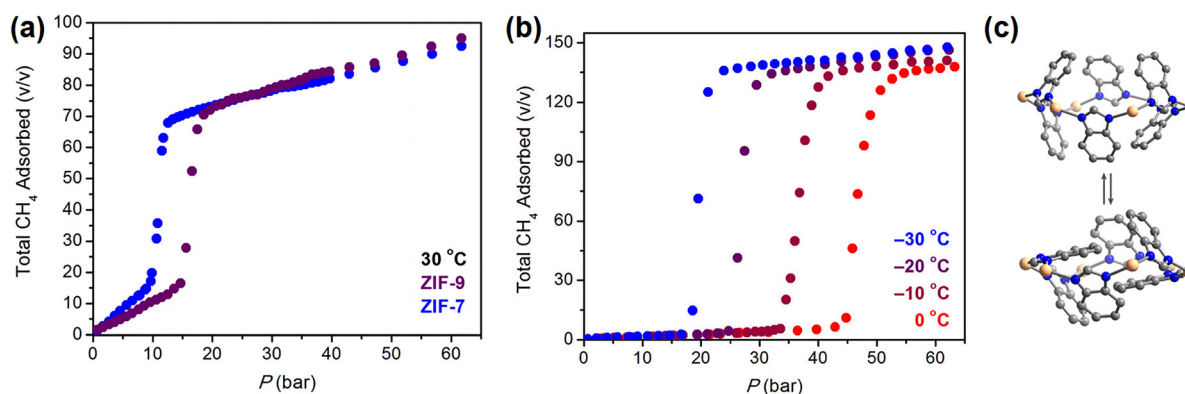


**FIG. 18.** (a) CH<sub>4</sub> uptake in Zn(bim)<sub>2</sub>/ZIF-7 (blue) and Co(bim)<sub>2</sub>/ZIF-9 (purple) at 30 °C (b) CH<sub>4</sub> uptake in Cd(bim)<sub>2</sub>/CdIF-13 at -30, -20, -10, and 0 °C. (c) Illustration of gate-opening effect in Cd(bim)<sub>2</sub>, with the open (top) and closed (bottom) pore configurations of the hexagonal aperture. Reproduced with permission from McGuirk *et al.*, *J. Am. Chem. Soc.* **140**, 15924–15933 (2018). Copyright 2018 American Chemical Society.

dichloromethane loaded closed-pore structure of Cd(bim)<sub>2</sub> has been obtained via x-ray powder diffraction. This structure exhibits linker rotation about the hexagonal pore aperture relative to the open form, resulting in a gate-closure effect [Fig. 18(c)]. This result is in line with the predicted transition behavior of Zn(bim)<sub>2</sub><sup>51</sup> as well as solvent-free closed-pore structure reported for the same analogue.<sup>52</sup>

### C. Photo-catalyzed shifting

Photo-catalyzed phase transitions in MOFs have been less well explored than those susceptible to other types of induction and fewer yet in regard to methane sorption. Nevertheless, photo-induced conformational effects do have the potential to impact methane sorption in MOFs. Notably, conformational shifts in such systems are not responsive to sorbate induction, and thus, the typical working capacity calculation of viable uptake is no more likely to be favorable than in a fully rigid structure. Rather, the sorption capacity under useful conditions in such a system would be obtained by photo-excitation to the most favorable structure for sorption uptake prior to exposure to pressurized gas to load. The release of the sorbate would, in addition to a decrease in pressure, involve the photo-induction a conformational shift to the less favorable structure. As such, the true “working capacity” would be the difference between the high loading structure at 65 atm and the 5 atm low loading structure at ambient temperature.

It should be noted, however, that some additional complications exist for the application of such materials to the storage of methane as a viable fuel source, most notably the technical implementation of a simple excitation method for use in any viable storage systems. No method of achieving complete photo excitation of MOF powder densely packed in a commercially viable tank system has been published in the literature. Another potential issue is the lifetime of the higher energy conformations in those systems with insufficiently high energy barriers to prevent inter-conversion without photonic excitation. These issues make practical implementation of these systems for gas sorption applications unfeasible without significant further research and is included herein solely as a concept study.

In 2012, Modrow *et al.* used post synthetic modification to produce two variants of Cr-MIL-101-NH<sub>2</sub>, a structure composed of Cr<sup>3+</sup> ions coordinated to amine functionalized 1,4-benzene dicarboxylate

linkers. The two novel structures, Cr-MIL-101-amide and Cr-MIL-101-urea, had partial replacement of the amine functionality with *p*-phenylazobenzoyl and 4-(phenylazo)phenylisocyanate functionality, respectively (Fig. 19).<sup>53</sup> The inclusion of azobenzene in these pendant groups provides the opportunity to examine the impact on methane uptakes of the well-known photo-catalyzed *trans/cis* transitions across the nitrogen double bond in these structures, though no high-pressure methane isotherm data have been published to date.

Transitions in both structures were confirmed using UV-Vis spectroscopy with switching wavelengths of 365 and 455 nm to induce the *cis* and *trans* conformations, respectively. Notably, in neither structure was full reversibility achieved. Speculative reasons for this include steric hindrances and photo-bleaching effects. In both cases, no significant evidence of spontaneous back switching from the *cis* to *trans* states was observed at room temperature over a 16-h period indicating a long half-life and potential suitability for sorption applications.<sup>53</sup>

Probing both the *trans* and *cis* conformations for methane sorption revealed that an increase in the concentration of *cis* isomerized pendant groups resulted in an increase in methane uptake of both structures in comparison with the *trans*-dominated variants. Sorption measurements in Cr-MIL-101<sub>amide</sub> immediately after activation produced uptake significantly lower than the subsequently *cis* catalyzed variant and significantly higher than the catalyzed *trans*-dominated structure. Succeeding applications of catalyzing wavelengths produced results with similar but muted results due to the incomplete reversibility of the system, with uptakes more closely in line with the initial structure [Fig. 20(a)].

Methane uptake measurements in Cr-MIL-101<sub>urea</sub> produced somewhat less straightforward results. The activated structure was found to have considerably lower uptake than the subsequently *cis* catalyzed structure as expected. The *trans* catalyzed structure, however, also produced uptakes in excess of the initial activated structure (though still somewhat lower than the *cis*-dominated variant). Furthermore, inter-conversion from the *trans* back to the *cis* resulted in a greater uptake than observed in the original *cis* structure measurement. Reconverting to the *trans* dominated structure, resulted in a drop in uptake, yet still sorbed higher amounts even than those of the original *cis* uptake [Fig. 20(b)].

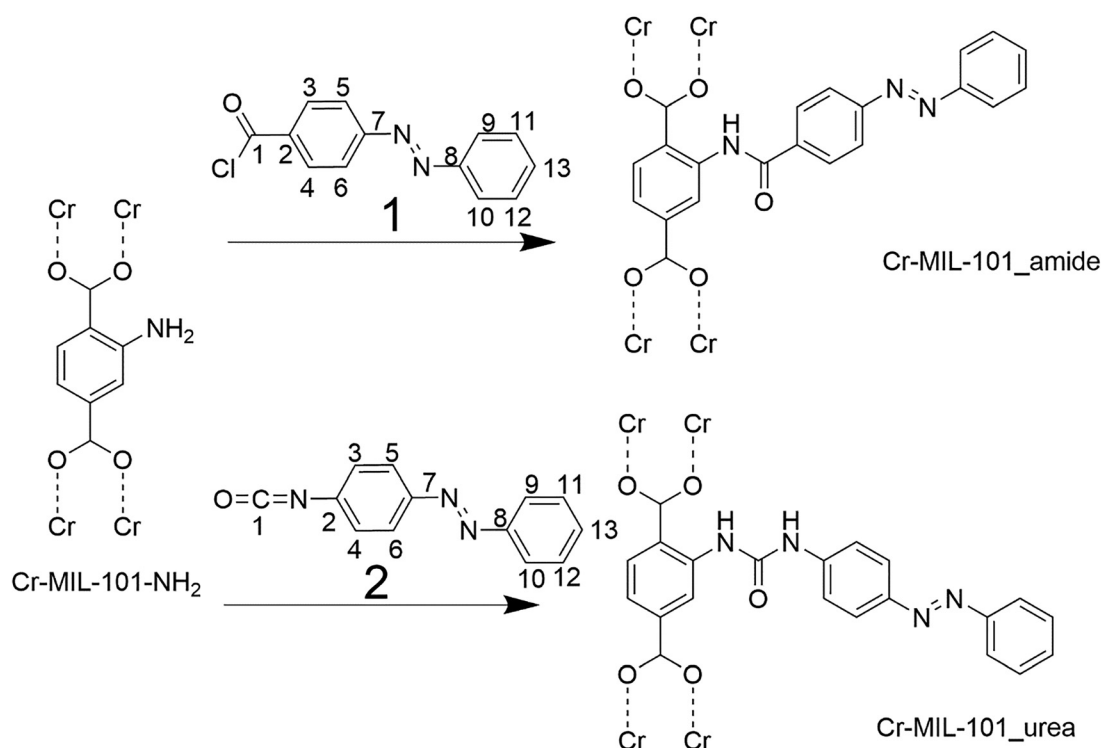


**FIG. 19.** Reaction schemes to obtain Cr-MIL-101-amide and Cr-MIL-101-urea from the post-synthetic modification of Cr-MIL-101-NH<sub>2</sub>. Reproduced with permission from Modrow *et al.*, *Dalton Trans.* **41**, 8690–8696 (2012). Copyright 2012 Royal Society of Chemistry.

While the origin of this continual increase in uptake in the Cr-MIL-101\_urea as the result of subsequent activation remains mysterious, it is nevertheless apparent in both structures that activation to a *cis*-dominated conformation increases uptake in comparison with the *trans*-dominated variant. Methane sorption in the commercially viable 5–65 atm range remains unexplored, however, and it is unclear whether conformational shifting of the bulky pendant groups would be possible with the steric barriers imposed by the presence of methane loaded at saturation densities.

#### IV. COMPUTATIONAL STUDIES

Computational techniques have long been a staple of MOF-sorption experimentation, providing insight into phenomena difficult or impossible to observe through purely wet lab techniques. The addition of MOF flexibility, however, has introduced some unique complications in traditional methodology as well as novel areas of investigation.

Classical modeling of MOF sorption is a computationally inexpensive technique which provides inter-molecular insights such as

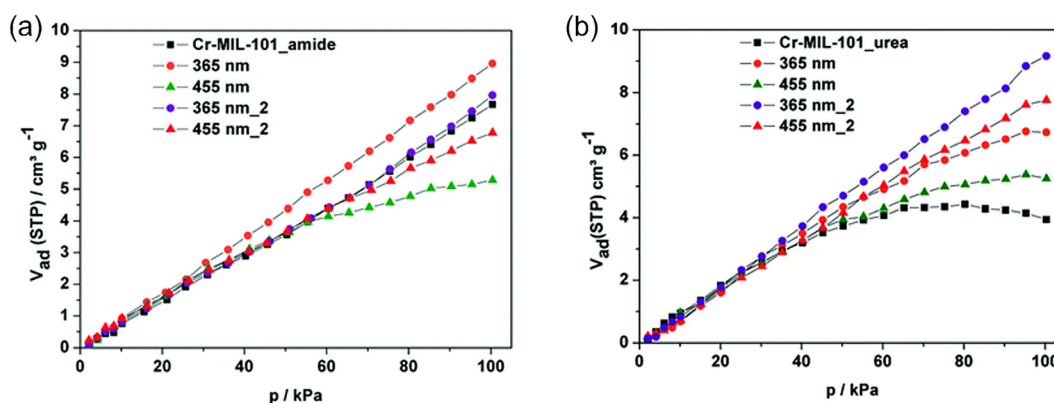


**FIG. 20.** Methane uptakes in the activated Cr-MIL-101\_amide (a) and Cr-MIL-101\_urea (b) structure and then after subsequent activation to the *cis* (365 nm excitation)- and *trans* (455 nm excitation)-dominated conformations. Reproduced with permission from Modrow *et al.*, *Dalton Trans.* **41**, 8690–8696 (2012). Copyright 2012 Royal Society of Chemistry.



binding sites/orientations (which can inform the design of superior structures), as well as wet lab observables such as uptakes. Typically, Monte Carlo (MC) and/or molecular dynamics methodologies are employed; the former providing uptakes under experimental conditions and observables obtainable through stochastic averaging and latter used to examine dynamic effects in MOF–sorbate interaction.

With flexible crystals, however, a difficulty arises. The stochastic nature of MC simulation makes the implementation of explicit framework flexibility generally unfeasible.<sup>54</sup> The obvious solution of separate examination of open and closed structures is frequently used, as in 2014 by Garcia-Perez *et al.* who matched open and closed phase simulated isotherms to different regions in the experimental curve and a linear combination of them to the transitional region between.<sup>55</sup> This adaption, however, is less well suited to the treatment of flexible MOFs without well-defined phases.<sup>56</sup> Krause *et al.* demonstrated that the solid–fluid interactions that drive framework deformation are strongly dependent on the isobaric–isothermal (NPT) ensemble.<sup>57</sup>

While MD calculations do not suffer from this flexibility limitation, it is difficult to explicitly implement fluctuation in sorbate number, which is particularly disadvantageous for flexible MOF simulation where the sorbate response opens the system to greater occupation in physical experimentation.

Therefore, a number of methods have been implemented to combine explicit framework flexibility with variation in particle number. Most notably, a number of hybrid MC/MD approaches have been applied, which alternate techniques, permitting particle fluctuation during the MC application and framework response in the MD phases. In 2019, Rogge *et al.* published a hybrid MC/MD technique and tested it against several existing algorithms on sorption in MIL-53(Al) of a series of gases, including methane. The novel approach obtained good agreement with experiment.<sup>56</sup>

Classical simulation is inherently limited not only by the quality of its force fields<sup>58</sup> but also by their classical nature for which electronic structure effects are approximated imperfectly or not at all. As such, quantum mechanical (QM) methods (typically density functional theory) are frequently employed after MC and/or MD to obtain accurate binding energies and orientations<sup>59,60</sup> and any other phenomena not tractable to classical treatment.

An emergent QM technique in MD simulation is *ab initio* molecular dynamics (AIMD). This method is identical to classical MD except that energy/force calculations are produced and recalculated as the simulation progresses from electronic structure calculations.<sup>61</sup> In addition to increased accuracy of calculations in comparison with its classical counterpart, AIMD can model electronic effects such as bond formation or breakage. QM treatment of forces is particularly useful for the study of flexible MOF systems as the explicit modeling of framework response without the limitations of static force fields provides more accurate conformational shifting. This was shown by Chen *et al.* who in 2013 studied MIL-53(Sc) with AIMD simulations; probing temperature induced shifts in the empty structure that had been reported from wet lab experimentation. X-ray crystal structures were reproduced with reasonable fidelity.<sup>58</sup>

A point of interest in flexible MOF methane storage research is in probing the reaction pathway between open- and closed-pore configurations. Elucidating mechanisms and potential energy barriers involved aids in tuning transition conditions to maximize uptake under optimal application conditions. Nudged elastic band (NEB)

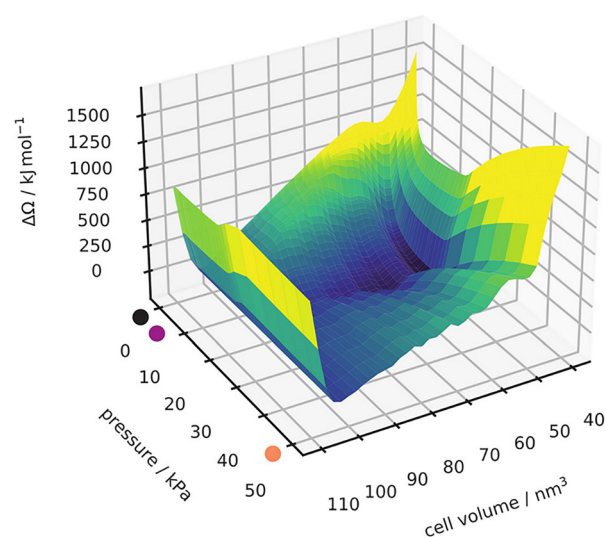


FIG. 21. Potential surface of DUT-49 at 120 K, as a function of methane pressure and unit cell volume. Reproduced with permission from Goeminne *et al.*, *J. Am. Chem. Soc.* **143**, 4143–4147 (2021). Copyright 2021 American Chemical Society.

calculations, a widely used method for finding reaction pathways and saddle points for reactions<sup>62</sup> and tractable to both classical and QM techniques, have been applied to flexible MOFs, as in 2019 by Yu *et al.* who used NEB to plot the conformational trajectory between the solvated and desolvated forms of NKU-FlexMOF-1.<sup>63</sup>

The plotting of energy barriers along these reaction trajectories has yet been little explored in simulation, but in 2021 Geominn *et al.* used hybrid MC/MD to map the energy landscape of DUT-49 successfully illustrating the origin of the negative gas sorption in the methane isotherm as pressure increases (Fig. 21).<sup>54</sup>

An avenue of investigation, which to the best of our knowledge, remains unexplored is the large-scale screening of flexible MOFs for any sorption applications, of both existing and hypothesized structures. Such studies have been performed on rigid crystals,<sup>64</sup> but the greater complexities of sorption in flexible systems make this type of investigation currently unfeasible. However, progress toward that goal has been made, such as the work of Sarkisov *et al.* published in 2014, who provided a simple algorithm for determining the flexibility of MOF structures providing a necessary first step for screening.<sup>27(b)</sup>

## V. DISCUSSION

It is notable that flexibility in MOFs with regard to non-methane sorbates has been better explored with a large number of flexible structures synthesized and examined.<sup>27</sup> Application of these systems to methane storage, however, is not straightforward as MOFs, which undergo conformational shifts in response to other sorbates, do not necessarily respond similarly to methane stimulation due to relatively non-polar and largely spherical nature of the latter. In the case of many sorbates currently examined for MOF sorption, such as carbon dioxide and water, high partial charges and shape directionality of the molecules provide opportunities for interaction with framework functionality. These interactions can provide structural facilitation for

conformational transitions.<sup>65–67</sup> However, as the molecular quadruple of methane is weak and the molecular shape creates little variation in interaction due to sorbate orientation, framework transitions are typically only observed in structures responsive to applied gas pressure under the given set of conditions. As such, the wide pool of flexible structures discussed in the literature is significantly narrowed for the purposes of methane sorption, under conditions relevant for methane storage application (e.g., pressure and temperature). A significant number of these systems, however, remain unexamined for methane applications and require further investigation. We note that the flexibility of MOFs is strongly dependent on the adsorption conditions and the nature of the gas that is being adsorbed. Thus, a single framework type might behave as both a rigid or flexible framework depending on the conditions and adsorbate.

In addition to the high uptake, ideal methane adsorbents for energy applications should have large differences in uptake between 5 and 65 atm under ambient temperatures; the conditions under which such energy storage systems will be expected to operate. One reason flexible MOFs are promising for such applications is due to the potential to chemically modify the frameworks to undergo phase shift in the desired pressure range making the most out of the difference in sorption favorability between closed- and open-pore conformations. Generally, the pore volume and density of the full open structure are taken into account to evaluate the total uptake and the deliverable capacities. However, in the case of materials exhibiting multi-step adsorption isotherm, it gets more complicated especially when the structure is not fully opened and it is reasonable to approximate the pore volume to the fully open structures but more reliable methods need to be developed.

It has been observed that it is possible to tune the flexation range of structures through the use of metal substitution such as observed in methane sorption in the bdp and MIL-53 series (Figs. 4 and 11). However, though electronegativity and ionic radii may have an impact, the effects of metal substitution on gate opening are largely dependent on the interaction of electron configuration of the ion with the geometry about the metal.<sup>68,69</sup> Contractions/elongations of bonds, and distortions of the bonding orientations will act to favor or disfavor conformational shifts. Due to the stereo-specific nature of these effects, metal substitutions must be considered on a case-by-case basis. It should also be noted that otherwise flexible MOFs, which do not respond to methane induction, might be primed to do so by careful metal substitution to make structural rearrangement more facile. This can be observed in the MIL-53 series in which the aluminum and chromium variants have type I isotherm in response to methane exposure, while the iron variant undergoes several conformational shifts.

The substitution of metal ions can also have an effect on the uptake. In addition to the obvious impact on gravimetric uptakes of replacing an ion with a lighter counterpart, the same effects of steric and bond length adjustments can affect uptakes. Nevertheless, these effects are more likely to be minor except in those systems where a conformational shift is made susceptible to methane induction or the same is inhibited. Thus, this strategy is more applicable to gate-opening as discussed above.

The other obvious area for tuning conformational shift conditions is linker modification. While gross alterations effectively create a novel system, and almost certainly impact uptake, small alterations such as

single-atom replacements can tune pore opening with negligible effect on uptake as observed with the replacement of hydrogen with fluorine in the flexible Co-bdp (Figs. 5 and 6).

It should not be assumed, however, that even minor alterations will not affect uptakes as they can result in potentially significant changes, as seen for UTSA-76 in comparison with its parent compound (Fig. 16). Addition of electronegative functionality can also increase uptake through favorable sorbate–structure interaction, while the introduction of mobile elements can result in an open structure better tuned to methane capacity, or indeed can introduce flexation into an otherwise rigid system. In both cases, however, the addition of functionality can inhibit conformational shifting either by creating new structural attachment energetics or through steric hindrance due to the presence of introduced functionality.

The use of computational experimentation to examine potential methane adsorbents has to date been somewhat underutilized despite the high value of the insight provided. From a basic practicality standpoint, the ability to modify extant MOFs and test the performance properties of such systems without the difficulty of physical synthesis allows a screening process, which can potentially expedite the experimentation process significantly. Examination of the crystal structures themselves and associated structural free energy differentials between crystal phases and along their conformational pathways can yield insight into which hypothetical structures are likely to be tractable to conformational shifting under imposed pressurized methane. Furthermore, the rational design of superior systems requires an atomistic level understanding of the processes involved, which can be difficult and sometimes impossible to obtain through wet lab investigation, can be obtained through careful simulation of the pertinent systems. Indeed, in some systems responsive motions in MOF frameworks may not be obvious without molecular level insight, as in the case of some systems with potential locally mobile elements.

## VI. CONCLUSION

This review is intended to elucidate the current state of affairs regarding the examination and use of flexibility in MOFs to enhance practical methane storage for energy storage applications. The field is still in its infancy, largely contained to modifications of a small number of MOF platforms and a few more individual systems.

No MOF structure, rigid or flexible, has yet been able to meet the DOE's current targets for viable methane on-board storage systems in terms of deliverable capacity. The target working capacity value of  $350 \text{ cm}^3 \text{ cm}^{-3}$  is a significant distance from the highest performing MOFs currently reported with uptakes in the vicinity of  $200 \text{ cm}^3 \text{ cm}^{-3}$  (Table 1). Flexible MOFs as an emerging class of porous materials with a potential for high deliverable capacity are thus, a promising class of materials that need further exploration and attention. The combination of theory and experiment will be vital in this regard to realize practical on-board methane storage and delivery at ambient conditions. Furthermore, research providing insights into the tank design capable of accommodating the volume changes in the framework would be crucial to realize these materials in on-board systems. Overall, the information provided in this review article can help guide scientists and engineers to gain new perspectives into creating novel porous materials that display improved  $\text{CH}_4$  uptake in the quest to meet the on-board  $\text{CH}_4$  storage targets set by the DOE.

TABLE I. Comparison of flexible MOFs with some representative robust MOFs for the high-pressure methane storage at room temperature.<sup>a</sup>

MOF	$D_c$ (g cm <sup>3</sup> cm <sup>-3</sup> )	$V_p$ (cm <sup>3</sup> g <sup>-1</sup> )	BET (m <sup>2</sup> g <sup>-1</sup> )	Total methane uptake		Methane working capacity <sup>b</sup>		$T$ (K)	$P$ (bar)	$T/P_{op}$ <sup>c</sup> (K/bar)	$Q_{st}$ (kJ mol <sup>-1</sup> ) <sup>d</sup>	References
				g g <sup>-1</sup>	cm <sup>3</sup> cm <sup>-3</sup>	g g <sup>-1</sup>	cm <sup>3</sup> cm <sup>-3</sup>					
Flexible frameworks												
Cu <sub>2</sub> (bdc) <sub>2</sub> (bpy)	0.791	0.261	700	0.056 <sup>e</sup>	62.5 <sup>e</sup>	0.052 <sup>e</sup>	58.2 <sup>e</sup>	298	35	298/9.0	NA	30
Cu(dhbc) <sub>2</sub> (bpy)	1.233	NA	320 <sup>f</sup>	0.055 <sup>e</sup>	98 <sup>e</sup>	0.054 <sup>e</sup>	93.7 <sup>e</sup>	298	65	298/8.0	NA	29
Cu(bpy) <sub>2</sub> (BF <sub>4</sub> ) <sub>2</sub>	NA	0.51	1426	0.061 <sup>g</sup>	NA	0.059 <sup>g</sup>	NA	303	63	303/38	13.0	31,70
MIL-53(Al)	0.978	0.54	1235	0.136 <sup>e</sup>	186 <sup>e</sup>	0.081 <sup>e</sup>	111 <sup>e</sup>	303	35	196/1.0	17	71,72
MIL-53(Fe)	NA	NA	NA	0.031 <sup>e</sup>	NA	0.030 <sup>e</sup>	NA	303	30	303/10	NA	32
MIL-53(Al)-NH <sub>2</sub>	1.02	0.50	947	0.085	121	0.081 <sup>h</sup>	115 <sup>h</sup>	298	65	298/24	NA	26(b)
MIL-53(Al)-OH	1.01	0.73	1284	0.155	217	0.118 <sup>h</sup>	164 <sup>h</sup>	298	65	298/15	NA	22
MIL-53(Al)-(OH) <sub>2</sub>	1.04	0.68	1193	0.066	96	0.051 <sup>h</sup>	71 <sup>h</sup>	298	65	298/53	NA	22
Co(bdp)	0.77	1.02	2911 <sup>f</sup>	0.187	203	0.183 <sup>h</sup>	197 <sup>h</sup>	298	65	298/16	13	6
Fe(bdp)	0.678	0.987	2780 <sup>f</sup>	0.206	196	0.200 <sup>h</sup>	190 <sup>h</sup>	298	65	298/24	11.8	6
Co(F-bdp)	0.726	0.88	2529 <sup>f</sup>	0.123 <sup>g</sup>	125 <sup>g</sup>	0.109 <sup>g</sup>	111 <sup>g</sup>	298	40	298/5.7	NA	28
Co(p-F <sub>2</sub> -bdp)	0.782	0.83	2279 <sup>f</sup>	0.113 <sup>g</sup>	124 <sup>g</sup>	0.110 <sup>g</sup>	120.5 <sup>g</sup>	298	40	298/10	NA	28
Co(o-F <sub>2</sub> -bdp)	0.739	0.95	2668 <sup>f</sup>	0.115 <sup>g</sup>	119 <sup>g</sup>	0.112 <sup>g</sup>	115.6 <sup>g</sup>	298	40	298/11	NA	28
Co(D <sub>4</sub> -bdp)	0.71	0.96	2702 <sup>f</sup>	0.128 <sup>g</sup>	128 <sup>g</sup>	0.126 <sup>g</sup>	126 <sup>g</sup>	298	40	298/18	NA	28
X-dia-1-Ni	0.85	0.62	1641 <sup>f</sup>	0.158	189	0.125	149	298	65	298/20	NA	35
DUT-49	0.312	2.91	5476	0.41	179	0.36	157	298	65	111/0.45	NA	37,38
Robust frameworks												
MOF-519	0.953	0.94	2400	0.19	259	0.15	210	298	65	NA	14.6	18
NJU-Bai-43	0.639	1.22	3090	0.283	254	0.221	198	298	65	NA	14.45	19
UTSA-76a	0.699	1.09	2820	0.263	257	0.201	197	298	65	NA	15	20
Fe-pbpta	0.376	2.15	4937	0.413	219	0.373	192	298	65	NA	22.27	73
MFM-115a	0.611	1.38	3394	0.278	238	0.223	191	298	65	NA	16.3	21
HKUST-1	0.883	0.78	1850	0.216	267	0.154	190	298	65	NA	17.0	15
MAF-38	0.761	0.808	2022	0.247	263	0.176	187	298	65	NA	21.6	17
MOF-905	0.549	1.34	3490	0.27	206	0.23	181	298	65	NA	11.7	74
Al-soc-MOF-1	0.34	2.3	5590	0.41	197	0.36	176	298	65	NA	11	75
NU-1500-Al	0.498	1.46	3560	0.29	200	0.24	165	296	65	NA	13.6	76

<sup>a</sup> $D_c$ : crystal density and  $V_p$ : pore volume.<sup>b</sup>The working capacity is defined as the difference in total uptake between 5 bars (or 5.8 bars<sup>b</sup>) and the specified upper limiting working pressure under isothermal conditions.<sup>c</sup> $T/P_{op}$ : gate open pressure with methane under specific temperature.<sup>d</sup>NA = Not available.<sup>e</sup>Not specified whether uptake is in terms of excess, total, or absolute adsorption.<sup>f</sup>Langmuir surface area.<sup>g</sup>Excess methane uptake value.<sup>h</sup>The specified upper limiting working pressure under isothermal conditions.

## ACKNOWLEDGMENTS

All authors gratefully acknowledge support from the Hydrogen and Fuel Cell Technologies and Vehicle Technologies Office within the U.S. Department of Energy's Office of Energy Efficiency and Renewable Energy (Award No. DE-EE0008812). B.S. acknowledges the National Science Foundation (Award No. DMR-1607989). S.M. acknowledges the Robert A. Welch Foundation (No. B-0027).

## AUTHOR DECLARATIONS

### Conflict of Interest

The authors have no conflicts to disclose.

## Author Contributions

K.A.F. and G.V. contributed equally to this work.

## DATA AVAILABILITY

The data that support the findings of this study are available within the article.

## REFERENCES

- <sup>1</sup>A. Qazi, F. Hussain, N. A. Rahim, G. Hardaker, D. Alghazzawi, K. Shaban, and K. Haruna, *IEEE Access* **7**, 63837–63851 (2019).
- <sup>2</sup>H. Li, K. Wang, Y. Sun, C. T. Lollar, J. Li, and H.-C. Zhou, *Mater. Today* **21**, 108–121 (2018).

- <sup>3</sup>D. Alezi, Y. Belmabkhout, and M. Eddaoudi, in *Elaboration and Applications of Metal-Organic Frameworks* (World Scientific, 2017), Vol. 2, pp. 207–246.
- <sup>4</sup>A. Schoedel, Z. Ji, and O. M. Yaghi, *Nat. Energy* **1**, 16034 (2016).
- <sup>5</sup>See <https://arpa-e.energy.gov/?q=programs/move> for information on the methane storage targets set by DOE.
- <sup>6</sup>J. A. Mason, J. Oktawiec, M. K. Taylor, M. R. Hudson, J. Rodriguez, J. E. Bachman, M. I. Gonzalez, A. Cervellino, A. Guagliardi, C. M. Brown, P. L. Llewellyn, N. Masciocchi, and J. R. Long, *Nature* **527**, 357–361 (2015).
- <sup>7</sup>Q. Wang and D. Astruc, *Chem. Rev.* **120**, 1438–1511 (2020); M. Safaei, M. M. Foroughi, N. Ebrahimpour, S. Jahani, A. Omid, and M. Khatami, *Trends Anal. Chem.* **118**, 401–425 (2019); S. Yuan, L. Feng, K. Wang, J. Pang, M. Bosch, C. Lollar, Y. Sun, J. Qin, X. Yang, P. Zhang, Q. Wang, L. Zou, Y. Zhang, L. Zhang, Y. Fang, J. Li, and H.-C. Zhou, *Adv. Mater.* **30**, 1704303 (2018).
- <sup>8</sup>B. Li, H.-M. Wen, W. Zhou, J. Q. Xu, and B. Chen, *Chem* **1**, 557–580 (2016); E. Mahmoud, L. Ali, A. El Sayah, S. A. Alkhatib, H. Abdulsalam, M. Juma, and A. A. H. Al-Muhtaseb, *Crystals* **9**, 406 (2019).
- <sup>9</sup>H. Furukawa, K. E. Cordova, M. O’Keeffe, and O. M. Yaghi, *Science* **341**, 1230444 (2013).
- <sup>10</sup>H.-C. Zhou, J. R. Long, and O. M. Yaghi, *Chem. Rev.* **112**, 673–674 (2012).
- <sup>11</sup>S. Ma and H.-C. Zhou, *Chem. Commun.* **46**, 44–53 (2010).
- <sup>12</sup>H. Li, M. Eddaoudi, M. O’Keeffe, and O. M. Yaghi, *Nature* **402**, 276–279 (1999).
- <sup>13</sup>M. Kondo, T. Yoshitomi, H. Matsuzaka, S. Kitagawa, and K. Seki, *Angew. Chem., Int. Ed.* **36**, 1725–1727 (1997).
- <sup>14</sup>M. Eddaoudi, J. Kim, N. Rosi, D. Vodak, J. Wachter, M. O’Keeffe, and O. M. Yaghi, *Science* **295**, 469–472 (2002).
- <sup>15</sup>S.-Y. Chui, S. M.-F. Lo, J. P. H. Charmant, A. G. Orpen, and I. D. Williams, *Science* **283**, 1148–1150 (1999); Y. Peng, V. Krungleviciute, I. Eryazici, J. T. Hupp, O. K. Farha, and T. Yildirim, *J. Am. Chem. Soc.* **135**, 11887–11894 (2013); X.-J. Hou, P. He, H. Li, and X. Wang, *J. Phys. Chem. C* **117**, 2824–2834 (2013).
- <sup>16</sup>S. Ma, D. Sun, J. M. Simmons, C. D. Collier, D. Yuan, and H.-C. Zhou, *J. Am. Chem. Soc.* **130**, 1012–1016 (2008).
- <sup>17</sup>J.-M. Lin, C.-T. He, Y. Liu, P.-Q. Liao, D.-D. Zhou, J.-P. Zhang, and X.-M. Chen, *Angew. Chem., Int. Ed.* **55**, 4674–4678 (2016).
- <sup>18</sup>F. Gándara, H. Furukawa, S. Lee, and O. M. Yaghi, *J. Am. Chem. Soc.* **136**, 5271–5274 (2014).
- <sup>19</sup>M. Zhang, W. Zhou, T. Pham, K. A. Forrest, W. Liu, Y. He, H. Wu, T. Yildirim, B. Chen, B. Space, Y. Pan, M. J. Zaworotko, and J. Bai, *Angew. Chem., Int. Ed.* **56**, 11426–11430 (2017).
- <sup>20</sup>B. Li, H.-M. Wen, H. Wang, H. Wu, M. Tyagi, T. Yildirim, W. Zhou, and B. Chen, *J. Am. Chem. Soc.* **136**, 6207–6210 (2014).
- <sup>21</sup>Y. Yan, D. I. Kolokolov, I. da Silva, A. G. Stepanov, A. J. Blake, A. Dailly, P. Manuel, C. C. Tang, S. Yang, and M. Schröder, *J. Am. Chem. Soc.* **139**, 13349–13360 (2017).
- <sup>22</sup>T. Kundu, B. B. Shah, L. Bolinoio, and D. Zhao, *Chem. Mater.* **31**, 2842–2847 (2019); J. Liang, X. Li, R. Xi, G. Shan, P.-Z. Li, J. Liu, Y. Zhao, and R. Zou, *ACS Mater. Lett.* **2**, 220–226 (2020).
- <sup>23</sup>Z. Chang, D.-H. Yang, J. Xu, T.-L. Hu, and X.-H. Bu, *Adv. Mater.* **27**, 5432–5441 (2015).
- <sup>24</sup>J. D. Evans, S. Krause, S. Kaskel, M. B. Sweatman, and L. Sarkisov, *Chem. Sci.* **10**, 5011–5017 (2019).
- <sup>25</sup>Z.-L. Shi and Y.-B. Zhang, *Isr. J. Chem.* **58**, 985–994 (2018); S. Hiraide, Y. Sakanaka, H. Kajiro, S. Kawaguchi, M. T. Miyahara, and H. Tanaka, *Nat. Commun.* **11**, 3867 (2020); D. Alezi, I. Spanopoulos, C. Tsangarakis, A. Shkurenko, K. Adil, Y. Belmabkhout, M. O’Keeffe, M. Eddaoudi, and P. N. Trikalitis, *J. Am. Chem. Soc.* **138**, 12767–12770 (2016).
- <sup>26</sup>(a) N. Chanut, A. Ghoufi, M.-V. Coulet, S. Bourrelly, B. Kuchta, G. Maurin, and P. L. Llewellyn, *Nat. Commun.* **11**, 1216 (2020); (b) L. Bolinoio, T. Kundu, X. Wang, Y. Wang, Z. Hu, K. Koh, and D. Zhao, *Chem. Commun.* **53**, 8118–8121 (2017); (c) A. Schneemann, V. Bon, I. Schwedler, I. Senkovska, S. Kaskel, and R. A. Fischer, *Chem. Soc. Rev.* **43**, 6062–6096 (2014); (d) T. Kundu, M. Wahiduzzaman, B. B. Shah, G. Maurin, and D. Zhao, *Angew. Chem., Int. Ed.* **58**, 8073–8077 (2019); (e) X. Yang, L. Si, G. Xie, L. Zhang, D. Guo, and J. Luo, *Comput. Mater. Sci.* **177**, 109543 (2020).
- <sup>27</sup>(a) J. H. Lee, S. Jeoung, Y. G. Chung, and H. R. Moon, *Coord. Chem. Rev.* **389**, 161–188 (2019); (b) L. Sarkisov, R. L. Martin, M. Haranczyk, and B. Smit, *J. Am. Chem. Soc.* **136**, 2228–2231 (2014); (c) N. Aljammal, C. Jabbour, S. Chaemchuen, T. Juzsakova, and F. Verpoort, *Catalysts* **9**, 512 (2019); (d) S. S. Nagarkar, A. V. Desai, and S. K. Ghosh, *Chem. Asian J.* **9**, 2358–2376 (2014).
- <sup>28</sup>M. K. Taylor, T. Runčevski, J. Oktawiec, M. I. Gonzalez, R. L. Siegelman, J. A. Mason, J. Ye, C. M. Brown, and J. R. Long, *J. Am. Chem. Soc.* **138**, 15019–15026 (2016).
- <sup>29</sup>R. Kitaura, K. Seki, G. Akiyama, and S. Kitagawa, *Angew. Chem., Int. Ed.* **42**, 428–431 (2003).
- <sup>30</sup>K. Seki, *Phys. Chem. Chem. Phys.* **4**, 1968–1971 (2002).
- <sup>31</sup>H. Noguchi, A. Kondoh, Y. Hattori, H. Kanoh, H. Kajiro, and K. Kaneko, *J. Phys. Chem. B* **109**, 13851–13853 (2005).
- <sup>32</sup>P. L. Llewellyn, P. Horcajada, G. Maurin, T. Devic, N. Rosenbach, S. Bourrelly, C. Serre, D. Vincent, S. Loera-Serna, Y. Filinchuk, and G. Férey, *J. Am. Chem. Soc.* **131**, 13002–13008 (2009).
- <sup>33</sup>T. Ahnfeldt, D. Gunzelmann, T. Loiseau, D. Hirsemann, J. Senker, G. Férey, and N. Stock, *Inorg. Chem.* **48**, 3057–3064 (2009).
- <sup>34</sup>S. Couck, J. F. M. Denayer, G. V. Baron, T. Remy, J. Gascon, and F. Kapteijn, *J. Am. Chem. Soc.* **131**, 6326–6327 (2009).
- <sup>35</sup>Q. Y. Yang, P. Lama, S. Sen, M. Lusi, K. J. Chen, W. Y. Gao, M. Shivanna, T. Pham, N. Hosono, S. Kusaka, J. J. Perry, S. Q. Ma, B. Space, L. J. Barbour, S. Kitagawa, and M. J. Zaworotko, *Angew. Chem., Int. Ed.* **57**, 5684–5689 (2018).
- <sup>36</sup>S. K. Elsaidi, M. H. Mohamed, L. Wojtas, A. Chanthapally, T. Pham, B. Space, J. J. Vittal, and M. J. Zaworotko, *J. Am. Chem. Soc.* **136**, 5072–5077 (2014).
- <sup>37</sup>U. Stoeck, S. Krause, V. Bon, I. Senkovska, and S. Kaskel, *Chem. Commun.* **48**, 10841–10843 (2012).
- <sup>38</sup>S. Krause, V. Bon, I. Senkovska, U. Stoeck, D. Wallacher, D. M. Többsen, S. Zander, R. S. Pillai, G. Maurin, F. X. Coudert, and S. Kaskel, *Nature* **532**, 348–352 (2016).
- <sup>39</sup>J. D. Evans, L. Bocquet, and F. X. Coudert, *Chem* **1**, 873–886 (2016).
- <sup>40</sup>S. Krause, J. D. Evans, V. Bon, I. Senkovska, F.-X. Coudert, D. M. Többsen, D. Wallacher, N. Grimmd, and S. Kaskel, *Faraday Discuss.* **225**, 168–183 (2012).
- <sup>41</sup>S. Krause, J. D. Evans, V. Bon, I. Senkovska, P. Iacomi, F. Kolbe, S. Ehrling, E. Troschke, J. Getzschmann, D. M. Többsen, A. Franz, D. Wallacher, P. G. Yot, G. Maurin, E. Brunner, P. L. Llewellyn, F.-X. Coudert, and S. Kaskel, *Nat. Commun.* **10**, 3632 (2019).
- <sup>42</sup>S. Krause, J. D. Evans, V. Bon, I. Senkovska, S. Ehrling, P. Iacomi, D. M. Többsen, D. Wallacher, M. S. Weiss, B. Zheng, P. G. Yot, G. Maurin, P. L. Llewellyn, F.-X. Coudert, and S. Kaskel, *Chem. Sci.* **11**, 9468–9479 (2020).
- <sup>43</sup>X. Lin, I. Telepeni, A. J. Blake, A. Dailly, C. M. Brown, J. M. Simmons, M. Zoppi, G. S. Walker, K. M. Thomas, and T. J. Mays, *J. Am. Chem. Soc.* **131**, 2159–2171 (2009).
- <sup>44</sup>W. Morris, C. J. Doonan, H. Furukawa, R. Banerjee, and O. M. Yaghi, *J. Am. Chem. Soc.* **130**, 12626–12627 (2008).
- <sup>45</sup>B. Zheng, F. Fu, L. L. Wang, L. Yang, Y. Zhu, and H. Du, *J. Phys. Chem. C* **122**, 7203–7209 (2018).
- <sup>46</sup>(a) K. S. Park, Z. Ni, A. P. Côté, J. Y. Choi, R. Huang, F. J. Uribe-Romo, H. K. Chae, M. O’Keeffe, and O. M. Yaghi, *Proc. Natl. Acad. U. S. A.* **103**, 10186–10191 (2006); (b) C. Zhang, R. P. Lively, K. Zhang, J. R. Johnson, O. Karvan, and W. J. Koros, *J. Phys. Chem. Lett.* **3**, 2130–2134 (2012).
- <sup>47</sup>V. T. Phuong, T. Chokbunpiam, S. Fritzsche, T. Remsungnen, T. Rungtongmongkol, C. Chmelik, J. Caro, and S. Hannongbua, *Microporous Mesoporous Mater.* **235**, 69–77 (2016).
- <sup>48</sup>X. Huang, J. Zhang, and X. Chen, *Sci. Bull.* **48**, 1531–1534 (2003).
- <sup>49</sup>A. Nogueira-Díaz, J. Villarroel-Rocha, V. P. Ting, N. Bimbo, K. Sapag, and T. J. Mays, *J. Chem. Technol. Biotechnol.* **94**, 3787–3792 (2019).
- <sup>50</sup>C. M. McGuirk, T. E. Runčevski, J. Oktawiec, A. Turkiewicz, M. K. Taylor, and J. R. Long, *J. Am. Chem. Soc.* **140**, 15924–15933 (2018).
- <sup>51</sup>Y. Du, B. Wooler, M. Nines, P. Kortunov, C. S. Paur, J. Zengel, S. C. Weston, and P. I. Ravikovitch, *J. Am. Chem. Soc.* **137**, 13603–13611 (2015).
- <sup>52</sup>P. Zhao, G. I. Lampronti, G. O. Lloyd, M. T. Wharmby, S. Facq, A. K. Cheetham, and S. A. Redfern, *Chem. Mater.* **26**, 1767–1769 (2014).
- <sup>53</sup>A. Modrow, D. Zargarani, R. Herges, and N. Stock, *Dalton Trans.* **41**, 8690–8696 (2012).

- <sup>54</sup>R. Goeminne, S. Krause, S. Kaskel, T. Verstraelen, and J. D. Evans, *J. Am. Chem. Soc.* **143**, 4143–4147 (2021).
- <sup>55</sup>E. García-Pérez, P. Serra-Crespo, S. Hamad, F. Kapteijn, and J. Gascon, *Phys. Chem. Chem. Phys.* **16**, 16060–16066 (2014).
- <sup>56</sup>S. M. J. Rogge, R. Goeminne, R. Demuyne, J. J. Gutiérrez-Sevillano, S. Vandenbrande, L. Vanduyfhuys, M. Waroquier, T. Verstraelen, and V. Van Speybroeck, *Adv. Theory Simul.* **2**, 1800177 (2019).
- <sup>57</sup>S. Krause, N. Hosono, and S. Kitagawa, *Angew. Chem., Int. Ed.* **59**, 15325–15341 (2020).
- <sup>58</sup>L. Chen, J. P. S. Mowat, D. Fairen-Jimenez, C. A. Morrison, S. P. Thompson, P. A. Wright, and T. Düren, *J. Am. Chem. Soc.* **135**, 15763–15773 (2013).
- <sup>59</sup>Z. Niu, X. Cui, T. Pham, P. C. Lan, H. Xing, K. A. Forrest, L. Wojtas, B. Space, and S. Ma, *Angew. Chem., Int. Ed.* **58**, 10138–10141 (2019).
- <sup>60</sup>D. G. Madden, D. O’Nolan, K.-J. Chen, C. Hua, A. Kumar, T. Pham, K. A. Forrest, B. Space, J. J. Perry, M. Khraisheh, and M. J. Zaworotko, *Chem. Commun.* **55**, 3219–3222 (2019).
- <sup>61</sup>R. Iftimie, P. Minary, and M. E. Tuckerman, *Proc. Natl. Acad. U. S. A.* **102**, 6654 (2005).
- <sup>62</sup>H. Jonsson, G. Mills, and K. W. Jacobsen, “Nudged elastic band method for finding minimum energy paths of transitions,” in *Classical and Quantum Dynamics in Condensed Phase Simulations* (World Scientific, 1998), pp 385–404.
- <sup>63</sup>M.-H. Yu, B. Space, D. Franz, W. Zhou, C. He, L. Li, R. Krishna, Z. Chang, W. Li, T.-L. Hu, and X.-H. Bu, *J. Am. Chem. Soc.* **141**, 17703–17712 (2019).
- <sup>64</sup>S. Lee, B. Kim, H. Cho, H. Lee, S. Y. Lee, E. S. Cho, and J. Kim, *ACS Appl. Mater. Interfaces* **13**, 23647–23654 (2021).
- <sup>65</sup>E. Stavitski, E. A. Pidko, S. Couck, T. Remy, E. J. Hensen, B. M. Weckhuysen, J. Denayer, J. Gascon, and F. Kapteijn, *Langmuir* **27**, 3970–3976 (2011).
- <sup>66</sup>S. Bourrelly, B. Moulin, A. Rivera, G. Maurin, S. Devautour-Vinot, C. Serre, T. Devic, P. Horcajada, A. Vimont, and G. Clet, *J. Am. Chem. Soc.* **132**, 9488–9498 (2010).
- <sup>67</sup>F. Salles, S. Bourrelly, H. Jobic, T. Devic, V. Guillerm, P. Llewellyn, C. Serre, G. Férey, and G. Maurin, *J. Phys. Chem. C* **115**, 10764–10776 (2011).
- <sup>68</sup>F. Salles, G. Maurin, C. Serre, P. L. Llewellyn, C. Knöfel, H. J. Choi, Y. Filinchuk, L. Oliviero, A. Vimont, J. R. Long, and G. Férey, *J. Am. Chem. Soc.* **132**, 13782–13788 (2010).
- <sup>69</sup>P. K. Thallapally, J. Tian, M. R. Kishan, C. A. Fernandez, S. J. Dalgarno, P. B. McGrail, J. E. Warren, and J. L. Atwood, *J. Am. Chem. Soc.* **130**, 16842–16843 (2008).
- <sup>70</sup>A. J. Blake, S. J. Hill, P. Hubberstey, and W.-S. Li, *J. Chem. Soc., Dalton Trans.* **1997**, 913–914.
- <sup>71</sup>P. Rallapalli, D. Patil, K. P. Prasanth, R. S. Somani, R. V. Jasra, and H. C. Bajaj, *J. Porous Mater.* **17**, 523–528 (2009).
- <sup>72</sup>A. Boutin, F.-X. Coudert, M.-A. Springuel-Huet, A. V. Neimark, G. Férey, and A. H. Fuchs, *J. Phys. Chem. C* **114**, 22237–22244 (2010).
- <sup>73</sup>G. Verma, S. Kumar, H. Vardhan, J. Ren, Z. Niu, T. Pham, L. Wojtas, S. Butikofer, J. C. Echeverria Garcia, Y.-S. Chen, B. Space, and S. Ma, *Nano Res.* **14**, 512–517 (2021).
- <sup>74</sup>J. Jiang, H. Furukawa, Y.-B. Zhang, and O. M. Yaghi, *J. Am. Chem. Soc.* **138**, 10244–10251 (2016).
- <sup>75</sup>D. Alezi, Y. Belmabkhout, M. Suyetin, P. M. Bhatt, Ł. J. Weseliński, V. Solovyeva, K. Adil, I. Spanopoulos, P. N. Trikalitis, A.-H. Emwas, and M. Eddaoudi, *J. Am. Chem. Soc.* **137**, 13308–13318 (2015).
- <sup>76</sup>Z. Chen, P. Li, R. Anderson, X. Wang, X. Zhang, L. Robison, L. R. Redfern, S. Moribe, T. Islamoglu, D. A. Gómez-Gualdrón, T. Yildirim, J. F. Stoddart, and O. K. Farha, *Science* **368**, 297 (2020).